Karlsruhe Institute of Technology

SCC Scientific Computing Center

Evaluation of Pulse Level Quantum Fourier Models

Bachelor's Thesis of

Tilmann Rothe Santos

At the KIT Department of Informatics
SCC - Scientific Computing Center

First examiner:	Prof. Dr. Achim Streit
First advisor:	M.Sc. Melvin Strobl
Second advisor:	Dr. Eileen Kuehn

22 January 2025 – 22 May 2025

Evaluation of Pulse Level Quantum Fourier Models (Bachelor's Thesis)

I declare that I have developed and written the enclosed thesis completely by myself. I have not used any other than the aids that I have mentioned. I have marked all parts of the thesis that I have included from referenced literature, either in their original wording or paraphrasing their contents. I have followed the by-laws to implement scientific integrity at KIT.

Karlsruhe, 22 May 2025

(Tilmann Rothe Santos)

Abstract

The promising field of Quantum Machine Learning (QML) widely employs Parametrized Quantum Circuits (PQCs). Specifically, PQCs whose output can be represented as a truncated Fourier series are often referred to as Quantum Fourier Models (QFMs). Using this representation enables the analysis through spectral properties, providing insights into the capability of PQCs to learn patterns in data. Typically, QFMs in this research area are conceptualized and implemented using gates, which serve as mathematical abstractions of quantum mechanical operations. This work moves beyond this abstract gate-level description by investigating if and how QFMs can be directly modeled at the pulse-level. This approach more accurately reflects the physical reality of quantum hardware, where gates are realized as electromagnetic pulses. The thesis at hand is concerned with both, theoretically derived and numerically validated framework, for constructing QFMs at the pulse-level. The provided framework grants increased control, due to the direct manipulation of pulse parameters, thereby laying a solid foundation for further investigations into the theoretical properties of QFMs.

Zusammenfassung

Das vielversprechende Feld des Quantenmaschinellen Lernens (QML) nutzt in großem Umfang parametrisierte Quantenschaltkreise (PQC). Insbesondere PQC, deren Ausgabe als abgeschnittene Fourier-Reihe dargestellt werden kann, werden oft als Quanten-Fourier-Modelle (QFM) bezeichnet. Diese Darstellung ermöglicht ihre Analyse anhand spektraler Eigenschaften, was wiederrum Einblicke in ihre Fähigkeit zum Erlernen von Datenmustern bietet. Typischerweise werden PQC in diesem Forschungsbereich mithilfe von Quanten-Gattern konzeptualisiert und implementiert, die als mathematische Abstraktionen quantenmechanischer Operationen dienen. Diese Arbeit geht über diese abstrakte Gatter-Ebene hinaus, indem sie untersucht, ob und wie PQC direkt auf der Pulsebene modelliert werden können. Dieser Ansatz spiegelt die physikalische Realität von Quantenhardware genauer wider, wo Gatter als präzise geformte elektromagnetische Pulse realisiert werden. Diese Abschlussarbeit bietet ein sowohl theoretisch abgeleitetes als auch numerisch implementiertes Framework zur Konstruktion von PQC auf der Pulsebene. Dieses Framework ermöglicht eine erhöhte Kontrolle durch die direkte Manipulation von Pulsparametern und legt somit eine solide Grundlage für weitere Untersuchungen der theoretischen Eigenschaften von QFM.

Contents

Abstract i

Zusammenfassung ii

1. Introduction 1

2. Preliminaries 3
2.1. Quantum Mechanics and Quantum Information . . . 3
2.1.1. Solving Quantum Dynamics . . . 4
2.1.2. Two-Level Systems . . . 6
2.1.3. Quantum Operations . . . 10
2.2. Pulse Control . . . 12
2.2.1. Quantum Hardware . . . 13
2.2.2. Pulse Level Elements . . . 13
2.3. Quantum Fourier Analysis . . . 15

3. Related Work 18
3.1. Noisy Intermediate-Scale Quantum Era . . . 18
3.2. Quantum Fourier Models . . . 19
3.2.1. Architectures . . . 19
3.2.2. Metrics and Limitations . . . 20
3.3. Pulse Level Modeling . . . 21

4. Methodology 23
4.1. Solving the Schrödinger Equation . . . 23
4.2. Static Hamiltonian . . . 24
4.3. Rotating frame . . . 25
4.4. Drive Hamiltonians . . . 26
4.4.1. X, Y - Rotations . . . 26
4.4.2. Z Rotation . . . 28
4.4.3. Hadamard . . . 29
4.4.4. Global Phase Factor . . . 30
4.5. Hamiltonians for Multiple States . . . 30
4.5.1. Single-Qubit Hamiltonian . . . 31
4.5.2. Independent Single-Qubit Hamiltonians . . . 31
4.6. Controlled NOT - A Two-Qubit Operator . . . 32
4.7. Numerical Validation . . . 34

4.8. Correlation Analysis 35

5. Results **39**
5.1. Simulation Frameworks 39
5.2. Numerical Implementation 40
5.3. Validation Experiments 41

6. Discussion **44**

7. Conclusion and Outlook **46**

Bibliography **48**

A. Appendix **59**
A.1. Notations 59
A.2. Pulse-Level Frameworks 60
A.3. Rotation Visualization 61

List of Figures

1.1. Gate-level vs. pulse-level quantum control of a QFM derived from the circuit expression. 2

2.1. Bloch sphere, illustrating its rotation axes (x, y, and z) which are orthogonal and intersect at the origin. A quantum state's position on the sphere is defined by its polar angle (θ) and azimuthal angle (φ). 7

4.1. Circuit diagram of Circuit 9 (C9), Circuit 15 (C15) from Ref [124] and the Hardware-Efficient Circuit (HEC) with circular entangling pattern. 36

5.1. Pseudocode of the *PulseBackend* class. 40
5.2. The gaussian function (a) modulated by the oscillating term (b) results in the control signal (c). 41

List of Tables

2.1. Comparison of closed and open quantum systems. 8

5.1. Number of pulses, as well as the Mean Absolute Error (MAE) before and after the correlation with the parameters for each circuit. 42
5.2. Correlation matrices for pulse-based evaluation and difference to the gate-based evaluation for each circuit. 43

A.1. Notation and description summary. 59
A.2. Collection of pulse-level programming frameworks. 60
A.3. Visualization of the trajectory of the populations and in the Bloch sphere for both the lab frame and rotating frame, caused by X-Rotations. 61

1. Introduction

Quantum computing leverages the principles of quantum mechanics, such as superposition and entanglement, to perform computations in ways that are fundamentally different from classical computers. This paradigm holds the promise for a number of highly valuable applications, including exponential speedup over classical methods, factor large numbers [122], or simulate quantum systems [73].

One promising branch of quantum computing is QML, which combines classical and quantum computational techniques to develop models for various machine learning tasks. For many QML tasks, Variational Quantum Algorithms (VQAs) are employed. These algorithms leverage classical optimizers for training [19], allowing them to adapt to specific problems. VQAs, in turn, rely on PQCs, which are quantum circuits whose operations depend on a set of adjustable parameters θ. One prominent research area is to analyze how expressive a PQC is its ability to generate entanglement, which are important metrics for determining its capability to learn complex functions and thus its potential performance in a given machine learning task [124]. In this work, we focus on a specific class of PQCs, namely QFMs, where the circuit follows a specific structure where the expectation value can be described as a truncated Fourier series. This perspective allows for the investigation of theoretical properties, such as the spectral analysis of the quantum circuit, which can then be used to quantify metrics like expressivity [83]. QFMs are composed of two main components, a variational ansatz which takes parameters $\boldsymbol{\theta}$ and an encoding block which takes the input feature x. The authors in Ref [119] showed that the coefficients c_ω depend on the trainable parameters $\boldsymbol{\theta}$ while the accessible spectrum Ω is determined by the data encoding components. In this setting, the Fourier series for the one-dimensional case can be written as the following equation:

$$f_{\boldsymbol{\theta}}(x) = \langle 0|^{\otimes n} U^\dagger(x,\boldsymbol{\theta}) \mathcal{M} U(x,\boldsymbol{\theta}) |0\rangle^{\otimes n} \overset{[119]}{=} \sum_{\omega\in\Omega} c_\omega(\boldsymbol{\theta}) e^{ix\omega}. \tag{1.1}$$

To evaluate quantum circuits, qubits in this research context are mostly manipulated by predefined gates. These gates are essentially built from unitary matrix multiplications, a mathematical abstraction of the underlying physics that governs the hardware systems. At the hardware level, most quantum circuits are ultimately realized as a series of precisely timed electromagnetic pulses [72, 64, 84].

The behavior of a quantum system under the influence of these pulses is fundamentally governed by the Schrödinger equation. This fundamental equation describes how the quantum state of a system changes over time, driven by its Hamiltonian. The Hamiltonian,

in essence, represents the total energy of the system and includes terms that describe the interaction of the quantum system with the applied microwave pulses. To precisely control the pulses and therefore, the Hamiltonian of a system, an additional set of parameters is required, which will here be referred to as pulse parameters $\mathbf{\Pi}$. These parameters directly influence properties such as the shape and length of the microwave pulse.

While pulse-level control introduces a lot of freedom, it demands a deep understanding of physics, time-consuming system modeling and substantial control resources. Yet, this significant complexity is precisely where its power lies. This otherwise challenging freedom becomes an advantage by offering finer control compared to the gate-level abstraction, as it increases the modeling capabilities. This increased capability is primarily used to mitigate the variety of errors that pose a major challenge in the NISQ era [95].

The objective is to verify if such QFMs can be evaluated at the pulse-level. Instead of the gate-level parameters $\boldsymbol{\theta}$, the additional set of pulse-level parameters $\mathbf{\Pi}$ is used to model an equivalent QFMs and to analyze its Fourier characteristics.

$$f_{\boldsymbol{\theta}}(x) = \sum_{\omega \in \Omega} c_\omega(\boldsymbol{\theta}) e^{ix\omega} \stackrel{?}{=} \sum_{\omega \in \Omega} c_\omega(\boldsymbol{\theta}, \mathbf{\Pi}) e^{ix\omega} =: f'_{\boldsymbol{\theta}, \mathbf{\Pi}}(x) \tag{1.2}$$

An illustration of this relationship is presented in Figure 1.1. Note that for the equivalence to hold, $\mathbf{\Pi}$ must be fixed. While exploring the correlation between $c_\omega(\boldsymbol{\theta})$ and $c_\omega(\boldsymbol{\theta}, \mathbf{\Pi})$ yields an interesting research direction, it is not an objective of this work.

$$\sum_{\omega \in \Omega} c_\omega(\boldsymbol{\theta}) e^{ix\omega} \stackrel{[119]}{=} \langle 0|^{\otimes n} U^\dagger(x, \boldsymbol{\theta}) \mathcal{M} U(x, \boldsymbol{\theta}) |0\rangle^{\otimes n} \qquad \text{Gate-Level (Abstract)}$$

$$\sum_{\omega \in \Omega} c_\omega(\boldsymbol{\theta}) e^{ix\omega} \stackrel{?}{=} \sum_{\omega \in \Omega} c_\omega(\boldsymbol{\theta}, \mathbf{\Pi}) e^{ix\omega} \qquad \text{Pulse-Level (Physical)}$$

Figure 1.1.: Gate-level vs. pulse-level quantum control of a QFM derived from the circuit expression.

This work therefore focuses on establishing the equivalence between the gate- and pulse-level formulations of quantum circuits. This equivalence is first derived theoretically, building from the foundational principles of quantum mechanics and an introduction to pulse control presented in Chapter 2. The mathematical derivations necessary for the construction of the required Hamiltonians to prove the equivalence are detailed in Chapter 4. The groundwork for Fourier analysis and QFMs is laid in Section 2.3 to establish the Fourier characteristics needed for comparing gate- and pulse-based evaluations in Section 4.8. Finally, this theoretical framework is validated through numerical simulations in Chapter 5 and its results are discussed in Chapter 6. The established equivalence aims to form a foundation for further analysis of the potential of modeling on pulse-level, as explored in Chapter 7.

Lastly, it is important to note that throughout this work the symbol Ω is used to denote two distinct concepts, standard within their respective domains. In the context of Fourier Analysis and QFMs, Ω represents the frequency spectrum. In contrast, when discussing pulse-level control, Ω refers to the Rabi frequency which will be formally introduced in Section 2.2.

2. Preliminaries

This chapter establishes the foundational principles essential for the methodology presented in the subsequent chapter. Initially, Section 2.1 delves into quantum mechanics, detailing its application in encoding and manipulating quantum information. Subsequently, Section 2.2 introduces pulse control, clarifying the operational principles of superconducting and trapped ion qubits, along with the physical elements needed for modeling and executing pulse control. The chapter concludes with Section 2.3, which provides an overview of fundamental Fourier analysis and specifies the structure and components of QFMs as they are utilized in this work.

2.1. Quantum Mechanics and Quantum Information

This section lays out the fundamental concepts for addressing quantum dynamics, as elaborated in Subsection 2.1.1. It then transitions to quantum information, introducing qubits as a consequence of physical properties in Subsection 2.1.2 and delving into the effects observed in real-world open quantum systems in Subsection 2.1.2.1. Basic mathematical concepts for forming (Subsection 2.1.2.2) and correctly notating (Subsection 2.1.2.3) multi-qubit states are also presented. Furthermore, Subsection 2.1.3 introduces quantum operations. Subsection 2.1.3.1 then specifies the gates necessary for a universal computational framework, while Subsection 2.1.3.2 details the crucial phenomenon of entanglement, using Bell states as a primary example.

Quantum mechanics is a fundamental mathematical framework, providing a set of postulates and rules for the construction of physical theories at the atomic and subatomic levels [86, 79]. Three notes underscore the foundational nature of quantum mechanics as a framework rather than a complete physical theory in itself.

- Quantum mechanics itself does not dictate the specific dynamical laws of a physical system. Rather, it provides the framework where laws, like the Schrödinger equation for non-relativistic systems, the Dirac equation for relativistic ones, or the Lindblad equation for open systems, must be formulated [12].
- Similarly, it's not quantum mechanics itself, but rather the specific physical system under consideration that dictates the nature of its state space, such as dimensionality and definition of the basis states [88]. For instance, a spin-1/2 particle has a 2-dimensional Hilbert space [28], whereas a harmonic oscillator possesses an infinite-dimensional one [69].

– Furthermore, Quantum mechanics itself doesn't directly tell us the specific state vector of a physical system at any given moment. Instead, determining how the state evolves over time, requires applying the system's specific dynamical laws to an initial state [86].

For any isolated physical system, there is a complex vector space with inner product (that is, a Hilbert space $\mathcal{H}$) known as the state space of the system. The system is completely described by its state vector, which is a unit vector in the system's state space [86].

The main discussion of this work will focus on closed systems. Analyzing closed systems can yield valuable insights of the underlying physical dynamics. Also analyzing closed systems is justified by the principle that any open system can be conceptually understood as a subsystem of a larger closed system, ultimately encompassing the Universe [86]. However, recognizing that open systems represent physical reality, they will be addressed in a later subsection.

2.1.1. Solving Quantum Dynamics

The evolution of a closed quantum system is described by a unitary operation. This means that the state $|\psi\rangle$ of the system at time t_0 is related to the state $|\psi(t)\rangle$ of the system at a later time t by a unitary operator $U(t, t_0)$ which depends only on the initial and final times t_0 and t [86].

$$|\psi(t)\rangle = U(t, t_0)|\psi\rangle. \tag{2.1}$$

The generator of this time evolution in quantum mechanics is the Hamiltonian operator, $\hat{H}$, which represents the total energy of the system. In the framework of quantum mechanics theories and experiments are required to determine the specific form of Hamiltonian for particular systems [86]. The fundamental equation governing the time evolution of the state vector is the Schrödinger equation [118]

$$i\hbar\frac{d}{dt}|\Psi(t)\rangle = \hat{H}|\Psi(t)\rangle \tag{2.2}$$

where $\hbar$ is the reduced Planck constant (also known as Dirac's constant).

Generally, the Hamiltonian operator can be time-dependent [106, 1], $\hat{H}(t)$, This time dependence is generally induced externally, e.g., by the dynamics in the environment of the system, or when a system is driven by external fields. Therefore systems with time-dependent Hamiltonian are often called *driven systems* [33, 117], leading to a time evolution described by:

$$i\hbar\frac{d}{dt}|\Psi(t)\rangle = \hat{H}(t)|\Psi(t)\rangle \tag{2.3}$$

Often, for simplicity, the reduced Planck constant $\hbar$ is set to one and absorbed into the Hamiltonian operator [86]. In this case, the Schrödinger equation can be formulated in the following form:

$$\frac{d}{dt}|\psi(t)\rangle = -i\hat{H}(t)|\psi(t)\rangle \tag{2.4}$$

In the time-independent case, we can look for solutions of the form $|\psi(t)\rangle = e^{-iEt/\hbar}|\psi\rangle$ [4] where E is the energy and $|\psi\rangle$ is a time-independent state vector. For these stationary states, the probability distributions of physical observables remain constant over time. Substituting this into the time-dependent Schrödinger equation yields the time-independent Schrödinger equation:

$$\hat{H}|\psi\rangle = E|\psi\rangle. \tag{2.5}$$

The solutions $|\psi\rangle$ to this equation are the energy eigenstates, which are also known as stationary states. Their time evolution only involves a global phase factor $e^{-iEt/\hbar}$, meaning that the probability distributions of physical observables remain constant over time.

There are two important properties of the Hamiltonian operator (for both time-independent and time-dependent) for physically realistic systems on a finite Hilbert space [85]:

- $H(t)$ is deterministic: For a given closed system, the Hamiltonian operator $H(t)$ is a well-defined and predictable function of time. This ensures that the time evolution of the quantum state is deterministic.
- $H(t)$ is Hermitian: The Hamiltonian operator $H(t)$ must be Hermitian (i.e., equal to its conjugate transpose, $H^\dagger(t) = H(t)$). This property ensures that the eigenvalues of the Hamiltonian, which represent the possible energy values of the system, are real and thus correspond to physically measurable quantities.

Because the Hamiltonian is a Hermitian operator, it has real eigenvalues (energies) and orthogonal eigenvectors (energy eigenstates). The spectral decomposition of a time-independent Hamiltonian is given by:

$$H = \sum_E E|E\rangle\langle E| \tag{2.6}$$

where E are the eigenvalues and $|E\rangle$ are the corresponding normalized energy eigenstates [86].

Given a system's Hamiltonian and Planck's constant $\hbar$, its dynamics are, in principle, fully determined. The dynamics can be solved analytically [104] or numerically [103, 96]. However, deriving the appropriate Hamiltonian for a specific physical system constitutes a significant challenge that has occupied a central role in twentieth-century physics [86].

Quantum dynamics can generally be analyzed from two primary approaches to analyzing quantum dynamics. The laboratory frame provides a typical inertial viewpoint where the observer is stationary relative to the experimental setup. In contrast, unitary transformations—a generalization of the Dirac picture [36]—allow us to shift this perspective to unitary

frames. These alternative frames can significantly simplify solving quantum evolution equations [115]. This simplification is often achieved by transforming the problem into a frame where specific time dependencies become more manageable or are eliminated entirely. A notable example of a unitary frame is the rotating frame, frequently employed when studying systems interacting with oscillating fields [5]. While the underlying physics of the simulation remains mathematically equivalent, solving problems in the rotating frame can lead to considerably faster computation times [24].

After transforming the Hamiltonian into the rotating frame other techniques like Rotating-wave approximation (RWA) [143] are used, where rapidly oscillating terms in the rotating frame Hamiltonian are neglected, further simplifying the problem [140].

2.1.2. Two-Level Systems

The simplest quantum mechanical system is the one consisting of two distinguishable energy levels, commonly referred to as a two-level system or a qubit in the context of quantum information, the associated state space is a two-dimensional complex Hilbert space, denoted as $\mathcal{H}_2$. The system's quantum state at any given time is represented by a state vector $|\psi\rangle$ within this Hilbert space [32]. A convenient and physically significant choice of orthonormal basis for this state space is given by the two eigenstates of a specific observable (often related to the energy or a measurement basis). These basis states are conventionally labeled as:

- $|0\rangle$ representing the ground state
- $|1\rangle$ representing the excited state

They are orthogonal, which ensures the independence of the energy eigenstates $\langle 0|1\rangle = 0$ and normalized $\langle 0|0\rangle = 1, \quad \langle 1|1\rangle = 1$. Consequently, any state vector $|\psi\rangle$ within this two-dimensional Hilbert space can be expressed as a linear superposition of these basis states:

$$|\psi\rangle = \alpha|0\rangle + \beta|1\rangle \tag{2.7}$$

Here $\alpha, \beta \in \mathbb{C}$ are the complex-valued coefficients. Subject to the normalization condition and according to the Born rule, the probability of outcome $|0\rangle$ with value "0" is $|\alpha|^2$ and the probability of outcome $|1\rangle$ with value "1" is $|\beta|^2$. Since these are probabilities for mutually exclusive and exhaustive outcomes, their sum must equal one:

$$|\alpha|^2 + |\beta|^2 = 1 \quad \text{which is equivalent to} \quad \langle\psi|\psi\rangle = 1. \tag{2.8}$$

Another useful representation of the state vector $|\psi\rangle$ is through the parametrization:

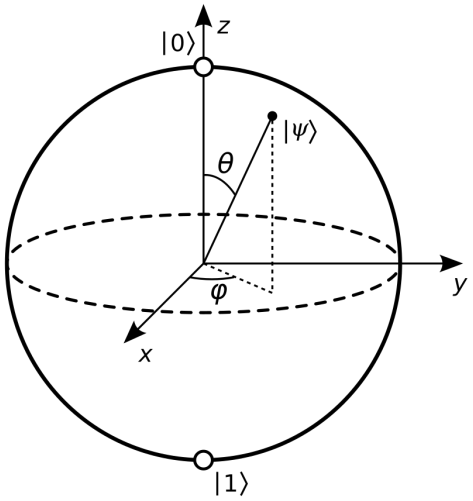

Figure 2.1.: Bloch sphere, illustrating its rotation axes (x, y, and z) which are orthogonal and intersect at the origin. A quantum state's position on the sphere is defined by its polar angle (θ) and azimuthal angle (φ).

$$|\psi\rangle = e^{i\gamma}\left(\cos\frac{\theta}{2}|0\rangle + e^{i\phi}\sin\frac{\theta}{2}|1\rangle\right) \tag{2.9}$$

In this representation, γ the global phase and $e^{i\gamma}$ is known as the global phase factor, which has no observable effect on the physical state of the system. The relative phase between the coefficients of the basis states is given by φ. This parametrization provides a convenient geometric interpretation of the state vector on the Bloch sphere, as illustrated in Figure 2.1, a geometrical representation of the pure state space of a two-level quantum mechanical system [9]. On the Bloch sphere, the state's position directly specifies its superposition and relative phase.

However, this intuition is limited to single-qubit state vectors. As will be introduced in Section 2.1.2.2, there is no straightforward generalization of the Bloch sphere to describe multi-qubit systems [86]. Furthermore, while two single-qubit states can always be combined using the tensor product to form a two-qubit state, not all two-qubit states can be expressed in this separable form, a phenomenon known as entanglement, which will be discussed later in Section 2.1.3.2. Additionally, the Bloch sphere provides a less direct representation for mixed states (described in Section 2.1.2.1, which are located in its interior [9]. Finally, it's worth noting that the Bloch sphere inherently discards global phase information, meaning that physically indistinguishable qubit states differing only by a global phase map to the same point on the sphere [9].

2.1.2.1. Open Systems

While idealized closed systems were discussed earlier, which exist primarily in simulation, perfectly isolated systems don't exist in reality. Real quantum technologies, such as today's

Noisy Intermediate-Scale Quantum (NISQ) computers which require external classical control for operations, inevitably interact with their environment, which can result in energy loss (dissipation) or energy gain (often leading to excitation). These unavoidable interactions manifest as noise in quantum information processing, causing deviations from ideal unitary evolution. In contrast to closed quantum systems, which undergo deterministic and purity-preserving unitary evolution, open systems experience non-unitary evolution due to environmental noise. The interaction with the environment introduces probabilistic elements and allows for the exchange of information and energy, meaning the system's evolution cannot be described by a reversible, norm-preserving unitary operation acting solely on its own state space [109].

The following describes several primary types of noise, for which further details can be found in the work of Nielsen et al. [86]. Decoherence, a general term for the loss of quantum information, occurs when qubits interact with the environment, causing them to lose their superposition and collapse into classical states. This includes energy relaxation, *T1 decay*, where the qubit loses energy and transitions from the excited state $|1\rangle$ to the ground state $|0\rangle$, and dephasing, *T2 decay*, where the qubit loses quantum phase information without energy loss, i.e. the relative phase between the $|0\rangle$ and $|1\rangle$ states becomes uncertain. Gate errors arise from imperfections in hardware or control pulses, causing quantum gates to deviate from their intended operations. Crosstalk happens when operations on one qubit unintentionally influence neighboring qubits due to their close proximity. Measurement errors can occur during the final state readout, leading to inaccuracies in the measured value. Additionally, environmental noise, such as thermal fluctuations, electromagnetic interference, and vibrations, can disturb quantum systems. Finally, control errors, stemming from pulse shape distortions and timing inaccuracies in the manipulation of qubits, introduce noise into quantum computations as well.

	Closed Systems	Open Systems
Governing Equation	Schrödinger equation	Lindblad equation
Quantum States	Pure states	Mixed states
Mathematical Representation	State vector $\|\psi\rangle$, Wave function $\|\psi\rangle$	Density operator $\hat{\rho}$
Bloch Sphere Visualization	State vector on the surface	State vector shrinks towards center
System Type	Idealized (Simulation)	Realistic (Noisy Intermediate Scale Quantum (NISQ))
Evolution	Unitary evolution	Non-unitary evolution
Errors	By definition	Leakage errors, State Preparation And Measurement (SPAM), decoherent and coherent noise

Table 2.1.: Comparison of closed and open quantum systems.

Although an ideal, perfectly isolated quantum computer is likely unattainable, the field of fault-tolerant quantum computing aims to develop methods and hardware architectures that can reliably perform quantum computations even in the presence of noise and errors inherent to open systems. By employing quantum error correction codes and fault-tolerant gate operations, the goal is to achieve scalable and reliable quantum computation despite the challenges posed by open system dynamics.

2.1.2.2. Composite Systems

The state space of a composite system is constructed by taking the tensor product, for matrices also known as the *Kronecker product* [46], of the state spaces of its individual components. This use of the tensor product is a widely accepted rule in quantum mechanics for describing composite systems [86]

Consider a system of n qubits. Each individual qubit has a 2-dimensional Hilbert space, $\mathcal{H}_i$ for $i = 1, 2, \ldots, n$. The state space of the composite n-qubit system, denoted by $\mathcal{H}$, is the tensor product of the individual qubit Hilbert spaces:

$$\mathcal{H} = \mathcal{H}_1 \otimes \mathcal{H}_2 \otimes \cdots \otimes \mathcal{H}_n \tag{2.10}$$

The dimension of this composite Hilbert space is 2^n. A basis for this space can be formed by taking the tensor product of the computational basis states of each qubit. For n qubits, these basis states are of the form

$$|x_1 x_2 \cdots x_n\rangle = |x_1\rangle \otimes |x_2\rangle \otimes \cdots \otimes |x_n\rangle \tag{2.11}$$

where each $x_i \in \{0, 1\}$. There are 2^n such basis states, corresponding to all possible n-bit binary strings. A general state $|\psi\rangle$ of an n-qubit system can be written as a superposition of these basis states

$$|\psi\rangle = \sum_{x_1 \in \{0,1\}} \sum_{x_2 \in \{0,1\}} \cdots \sum_{x_n \in \{0,1\}} c_{x_1 x_2 \cdots x_n} |x_1 x_2 \cdots x_n\rangle \tag{2.12}$$

where $c_{x_1 x_2 \cdots x_n}$ are complex coefficients satisfying the normalization condition:

$$\sum_{x_1 \in \{0,1\}} \sum_{x_2 \in \{0,1\}} \cdots \sum_{x_n \in \{0,1\}} |c_{x_1 x_2 \cdots x_n}|^2 = 1 \tag{2.13}$$

Operations on multi-qubit systems are described by unitary operators acting on the composite Hilbert space $\mathcal{H}$. These operators can act on individual qubits or can be entangling operations that affect multiple qubits simultaneously, creating correlations that have no classical analogue [86].

2.1.2.3. Conventions

For multi-qubit operations, the ordering of qubits within a register is important. Standard notations for the Most Significant Bit (MSB) and Least Significant Bit (LSB) are used [107]. There are two primary endian conventions prevalent in quantum computing [67].

Big-Endian: This convention associates the MSB of the encoded value with the lower index of the quantum register. Consequently, reading the qubits in the order of their indices (from lower to higher) effectively yields the encoded value from most significant to least significant bit (e.g., as used in the quantum programming framework *PennyLane* [53]). For example, for a two-qubit system, the state $|q_0 q_1\rangle$ would be represented as $|q_0\rangle \otimes |q_1\rangle$. When applying a two-qubit gate, the operator for the gate acting on qubits 0 and 1 would be represented as $G_{01} = G_{(0)} \otimes G_{(1)}$, where $G_{(0)}$ acts on qubit 0 and $G_{(1)}$ acts on qubit 1.

Little-Endian: The Little-Endian convention, in contrast, assigns the LSB to the lower index of the quantum register. Reading the qubits in the order of their indices thus yields the encoded value from least significant to most significant bit (e.g., as used in the quantum programming framework *Qiskit* [100]).

In this case, $|q_0 q_1\rangle$ would be represented as $|q_1\rangle \otimes |q_0\rangle$. The same two-qubit gate acting on qubits 0 and 1 would be represented as $G_{01} = G_{(1)} \otimes G_{(0)}$.

2.1.3. Quantum Operations

Quantum mechanics is inherently linear. A key constraint for quantum gates is that they must be unitary operators [86]. This ensures that quantum gates are always invertible, as the inverse of a unitary matrix is also unitary. Consequently, any quantum gate can always be reversed by applying another quantum gate. Furthermore, the space of possible quantum gates is vast, encompassing an uncountably infinite number of operations [141]. While an infinite number of quantum gates exist, practical quantum computing relies on a finite set for complex computations. The concept of universal quantum gate sets addresses this, showing how a select few gates can approximate any quantum computation to a desired accuracy, which is an important requirement for building practical quantum computers.

2.1.3.1. Universal quantum gate sets

In classical computation, a gate set is considered universal if any Boolean function on any number of bits can be expressed by combining a sufficient number of gates from that set. This property is crucial for hardware manufacturers as it allows them to optimize the design and manufacturing processes around a small number of fundamental gate types [86]. Analogously, a set of quantum gates is considered to be universal if it is possible to approximate any unitary transformation on any number of qubits to any desired degree of precision by composing gates from this set. The Solovay–Kitaev theorem provides a guarantee that such an efficient approximation is always possible [62]. Unlike classical computation, there

exists no common standard set of universal quantum gates. Instead, several different sets have been shown to be universal [141, 22].

For single-qubit operations, the Pauli X, Y, and Z gates, along with the Hadamard gate, can generate a dense set of rotations. This means that by combining these gates, we can approximate any arbitrary single-qubit rotation to a desired accuracy. When this set is extended by a two-qubit entangling gate, such as the CNOT gate, the resulting gate set $\{H, X, Y, Z, \text{CNOT}\}$ becomes universal and capable of approximating any quantum circuit acting on any number of qubits [78].

The Pauli matrices

$$I = \begin{pmatrix} 1 & 0 \\ 0 & 1 \end{pmatrix} \quad \sigma_x = \begin{pmatrix} 0 & 1 \\ 1 & 0 \end{pmatrix}, \quad \sigma_y = \begin{pmatrix} 0 & -i \\ i & 0 \end{pmatrix}, \quad \sigma_z = \begin{pmatrix} 1 & 0 \\ 0 & -1 \end{pmatrix} \tag{2.14}$$

are traceless, Hermitian, involutory and unitary[116]. Any matrix $\mathbb{C}^{2^n \times 2^n}$ can be decomposed as a linear combination of tensor products of the Pauli matrices [63].

The rotation gates around the X, Y, and Z axes are constructed using the Pauli matrices, they are defined as

$$R_x(\theta) = e^{-i\frac{\theta}{2}\sigma_x} = \cos\left(\frac{\theta}{2}\right) I - i \sin\left(\frac{\theta}{2}\right) \sigma_x = \begin{pmatrix} \cos(\theta/2) & -i\sin(\theta/2) \\ -i\sin(\theta/2) & \cos(\theta/2) \end{pmatrix} \tag{2.15}$$

$$R_y(\theta) = e^{-i\frac{\theta}{2}\sigma_y} = \cos\left(\frac{\theta}{2}\right) I - i \sin\left(\frac{\theta}{2}\right) \sigma_y = \begin{pmatrix} \cos(\theta/2) & -\sin(\theta/2) \\ \sin(\theta/2) & \cos(\theta/2) \end{pmatrix} \tag{2.16}$$

$$R_z(\theta) = e^{-i\frac{\theta}{2}\sigma_z} = \cos\left(\frac{\theta}{2}\right) I - i \sin\left(\frac{\theta}{2}\right) \sigma_z = \begin{pmatrix} e^{-i\theta/2} & 0 \\ 0 & e^{i\theta/2} \end{pmatrix} \tag{2.17}$$

where θ is the angle of rotation. The exponential of a matrix A is defined by its Taylor series expansion: $e^A = \sum_{n=0}^{\infty} \frac{A^n}{n!}$ [11]. For the Pauli matrices, since $\sigma_j^2 = I \quad$ for $j \in \{x, y, z\}$, the exponentials simplify to the forms shown above using Euler's formula.

The Hadamard gate is defined as

$$H = \frac{1}{\sqrt{2}} \begin{pmatrix} 1 & 1 \\ 1 & -1 \end{pmatrix} \tag{2.18}$$

and the Controlled-NOT (CNOT) gate is given by:

$$\text{CNOT} = \begin{pmatrix} 1 & 0 & 0 & 0 \\ 0 & 1 & 0 & 0 \\ 0 & 0 & 0 & 1 \\ 0 & 0 & 1 & 0 \end{pmatrix} \tag{2.19}$$

2.1.3.2. Entanglement

Quantum entanglement, one of the primary feature of quantum mechanics not present in classical mechanics [47], is the phenomenon where the quantum state of each particle in a group cannot be described independently of the state of the others, even when the particles are separated by a large distance [38]. Entangling capabilities are necessary for quantum circuits because they allow for the creation of complex superpositions and non-classical correlations between qubits. Without entanglement, the computational power of the quantum circuits would be severely limited, essentially reducing them to classical computations or offering only polynomial speedups [57].

Bell states, also referred to as *EPR* pairs, serve as a prime example and represent the simplest instances of quantum entanglement [86]. In these states, measuring one qubit instantaneously determines the outcome of measuring the other. The correlations observed in Bell states are stronger than any possible classical correlations, a foundational result demonstrated by John Bell [86]. There are four maximally entangled two-qubit Bell states, which form a maximally entangled basis known as the Bell basis:

$$|\Phi^+\rangle = \frac{1}{\sqrt{2}}(|00\rangle + |11\rangle) \tag{2.20}$$

$$|\Phi^-\rangle = \frac{1}{\sqrt{2}}(|00\rangle - |11\rangle) \tag{2.21}$$

$$|\Psi^+\rangle = \frac{1}{\sqrt{2}}(|01\rangle + |10\rangle) \tag{2.22}$$

$$|\Psi^-\rangle = \frac{1}{\sqrt{2}}(|01\rangle - |10\rangle) \tag{2.23}$$

2.2. Pulse Control

This section introduces pulse control, detailing the operational principles of superconducting qubits and trapped ion qubits in Subsection 2.2.1. Subsection 2.2.2 then focuses on the implementation of these systems, differentiating between components intrinsic to the physical system, which are discussed in Subsection 2.2.2.1, and the control elements necessary for state manipulation, described in Subsection 2.2.2.2. Finally, Subsection 2.2.2.3 presents useful approximation techniques for solving system dynamics.

At the fundamental level, pulses are at the implementation layer for quantum operations on most quantum hardware [127]. By precisely shaping electromagnetic pulses (like microwaves for superconducting, lasers for trapped ions), it offers significant advantages: finer control for optimizing performance, the design of quantum algorithms and hardware, and trainability [51], while also enabling error mitigation [108] and higher gate fidelity [130] [140]. Direct pulse programming can reduce latency by bypassing gate-level compilation redundancies [70] and minimize leakage from the qubit's computational space [137].

2.2.1. Quantum Hardware

The two leading platforms for quantum computing are superconducting and trapped ion qubits [72]. Both platforms rely on precisely shaped time-dependent electromagnetic fields (the pulses) that interact with the qubits according to a specific Hamiltonian. By modifying these pulses, we can control the quantum state evolution and implement the desired quantum operations. The details of the Hamiltonian and the nature of the control fields differ due to the distinct physical implementations of the qubits [2, 133].

Superconducting qubits are fabricated from superconducting materials that exhibit zero electrical resistance below a critical temperature, requiring cryogenic cooling[64, 111]. They function as artificial atoms with quantized energy levels, where the ground ($|0\rangle$) and first excited ($|1\rangle$) states serve as the qubit states. The energy difference between the $|0\rangle$ and $|1\rangle$ states defines the qubit's transition frequency. These circuits typically consist of inductors, capacitors (forming an LC oscillator), and a crucial non-linear element, the Josephson junction, which introduces anharmonicity necessary for defining the two-level system [94][2]. Microwave fields are used to induce oscillations in the circuit, transferring energy between the qubit's energy levels and thus manipulating its state vector [64]. Different types of superconducting qubits exist, such as charge, flux, and transmon qubits, with companies like Google and IBM notably utilizing the transmon architecture.

Trapped ion qubits utilize individual, charged atoms (ions) confined and suspended in a vacuum by precisely controlled electromagnetic fields. Quantum information is encoded within stable electronic energy levels of each ion, forming the $|0\rangle$ and $|1\rangle$ qubit states, often specifically in hyperfine (nuclear spin) states. The lowest level vibrational modes (phonons) of these trapped atoms also play a crucial role in their operation. The primary tool for manipulating trapped ion qubits is the application of laser pulses. These pulses induce transitions between the internal qubit states for single-qubit operations by externally manipulating the atomic state via the Jaynes-Cummings interaction. Entanglement between qubits is achieved by coupling the internal qubit states to a shared phonon state. Initial state preparation involves cooling the atoms (through trapping and optical pumping) into their motional ground state and hyperfine ground state [84, 7]. Arbitrary quantum transformations (unitary evolution) are constructed by applying sequences of these laser pulses. Prominent companies in this field include IonQ [20] and Quantinuum [21].

2.2.2. Pulse Level Elements

In pulse control, it is useful to distinguish between the elements that can be actively manipulated to shape the control pulses and the inherent properties of the physical system being controlled. Typically, the pulse shaping controls need to be tailored to the given system Hamiltonian properties to achieve the desired quantum interactions.

2.2.2.1. System Hamiltonian Properties

- Static Hamiltonian or system Hamiltonian H_{static} or H_0: Describes the intrinsic energy levels and interactions within the quantum system in absence of any external driving forces.
- Transition frequency or resonance frequency ω_q
- Reduced Planck's constant $\hbar$: A fundamental constant, $\hbar = \frac{h}{2\pi}$, whereas h closely related to $\hbar$ is a fundamental physical constant. $\hbar$ will continuously be set to one

The transition frequency, a fundamental characteristic of a qubit, arises from the natural energy difference between its discrete energy levels and is an intrinsic property determined by its physical implementation. This frequency can be expressed in several ways. As an angular frequency, denoted by ω_q and measured in radians per second, it represents the rate of oscillation associated with the energy transition. It is also sometimes referred to as ω_0, indicating a general characteristic frequency of a system. Alternatively, the transition frequency can be given as a standard frequency,ν_0, measured in Gigahertz, where the relationship between the angular and standard frequency is $\omega_q = 2\pi\nu_0$. The value of this transition frequency is precisely determined by Bohr's frequency condition, which establishes a direct relationship between the energy difference $\Delta E = E_1 - E_0$ between the qubit's energy levels and the frequency of the transition: $\Delta E = h\nu_0 = \hbar\omega_q$,

2.2.2.2. Pulse Shaping Controls

- Hamiltonian Operators or Control Operators H_j
- Control signals $S_j(t) = f(t)x(t) \quad \text{with} \quad |S_j(t)| \leq 1$ [140]
- Drive strength r in Gigahertz (GHz): This parameter, also referred to as the angular Rabi frequency ($\Omega = 2\pi r$ in radians per second), influences the rate of transitions in an oscillating electromagnetic field [42].
- Duration T and time steps dt: The length of the applied pulse $T * dt$, typically measured in nanoseconds (ns). Time steps dt is an important parameter in numerical simulations, determining the resolution of the time evolution.

The time-dependent drive Hamiltonian, $H_{\text{drive}}(t) = \sum_j S_j(t)H_j$, is constructed from a set of time-varying control signals, $S_j(t)$, that modulate corresponding time-independent Hamiltonian operators, H_j, thereby enabling active manipulation of the quantum system.

Hamiltonian operators are specific operators within the Hamiltonian that the control fields directly couple to. They determine which transitions or manipulations are induced in the quantum system by the applied control signal.

Control signals are constructed from two fundamental components: an envelope and a carrier wave. The envelope, often represented by a Gaussian or Gaussian-like pulse denoted

as $f(t)$, serves as the modulation of the control signal. This envelope dictates the time-dependent drive amplitude, A. Notably, Gaussian envelopes can be further shaped by a parameter σ, which defines the pulse's width or spread in the time domain. This parameter σ is therefore important when evaluating the system's temporal evolution.

The second key component is the carrier wave, $x(t)$, which provides the oscillatory nature of the control signal. This carrier wave is typically a sinusoid [140, 114]. The carrier wave itself is characterized by two primary parameters. First, the carrier frequency, ω_c, sometimes also referred to as ω_{LO} (local oscillator frequency), determines the rate at which the signal oscillates. For effective control, this carrier frequency is often selected to be near the qubit's transition frequency $\omega_c \approx \omega_q$ [31]. Second, the phase parameter, ϕ_c, provides an additional degree of freedom, allowing for precise control over the phase of the applied field.

2.2.2.3. Approaches to Solving Dynamics

In the analytical or numerical treatment of quantum dynamics, several approximations are commonly employed, as discussed in Subsection 2.1.1, to simplify the governing equations and reduce the computational demands. One prevalent technique involves the use of unitary transformations, such as the rotating frame transformation defined by $U(t) = \exp(-iH_{\text{static}}t/\hbar)$. This transformation shifts the analysis into a frame of reference that rotates at the frequency dictated by the static Hamiltonian, H_{static}.

Another widely used approximation is the Rotating-Wave Approximation (RWA). This approximation is typically valid under specific conditions, namely when the driving fields applied to the system are weak and when their frequencies are close to the resonant frequencies of the system on driven two-level systems [143]. Under these conditions, the RWA allows for the neglect of fast-oscillating terms in the Hamiltonian, leading to a significantly simplified description of the system's dynamics.

2.3. Quantum Fourier Analysis

By expressing a function as a sum of sines and cosines, many problems involving the function become easier to analyze because trigonometric functions are well understood [16].

A periodic function f with period P has a continuous Fourier series:

$$f(x) = \sum_{n=-\infty}^{\infty} c_n e^{i2\pi \frac{n}{P} x} \tag{2.24}$$

where the complex coefficients c_n are given by:

$$c_n = \frac{1}{T} \int_a^{a+T} f(x) e^{-i\frac{2\pi n}{T}x} dx \tag{2.25}$$

A truncated Fourier series approximating a P-periodic signal $s(x)$ with $N + 1$ frequency components can be written as:

$$s_N(x) = a_0 + \sum_{n=1}^{N} \left(a_n \cos\left(2\pi \frac{n}{P} x\right) + b_n \sin\left(2\pi \frac{n}{P} x\right) \right) \tag{2.26}$$

or equivalently in exponential form using Euler's formula ($e^{ix} = \cos x + i \sin x$):

$$s_N(x) = \sum_{n=-N}^{N} c_n e^{i2\pi \frac{n}{P} x} \tag{2.27}$$

When the signal is only known at discrete points, the Discrete Fourier Transform (DFT) becomes the appropriate tool for frequency analysis. For a set of discrete data points $s[x_p]$ at equally spaced points $\{\mathbf{x}_p\} := x_0, x_1, \ldots, x_{N-1}$ for a finite sequence of length N, the discrete Fourier Transform (DFT) [16] returns $\{\mathbf{C}_k\} := C_0, C_1, \ldots, C_{N-1}$:

$$C_k = \frac{1}{N} \sum_{p=0}^{N-1} s[x_p] e^{-\frac{i2\pi k}{N} p} \tag{2.28}$$

With a Capital C to distinguish from the continuous case [16].

Generally, for a real-valued input signal $\{\mathbf{x}_p\}$, the DFT coefficients exhibit a symmetry property: $C_i = \overline{C_{N-i}}$. This means that the information for frequencies k from $N/2$ to $N - 1$ is redundant, as it can be derived from the coefficients C_1 to $C_{\lfloor N/2 \rfloor - 1}$. Therefore, for a real-valued DFT, we typically only need to consider the unique coefficients from C_0 up to $C_{\lfloor N/2 \rfloor}$.

It's important to note that while the DFT yields N coefficients for a signal of length N, often only a subset M ($M \ll N$ of these coefficients carries significant information. The magnitude of the DFT coefficients serves as a primary indicator of their significance, with larger magnitudes typically corresponding to the dominant frequency components that contribute most to the signal's energy [16].

The Fast Fourier Transform (FFT) is an efficient algorithm to compute the DFT and its inverse (IDFT). DFT and FFT are often used interchangeably [16].

Building upon a foundational understanding of classical Fourier analysis, this section introduces QFM. It illustrates how the principles of frequency decomposition extend to the quantum realm, providing a new paradigm for data analysis.

Quantum Fourier Models, as originally described by Schuld [119], generally consider the input and frequency parameters as vectors. It's important to note that for the purposes of this project, the focus will be on the simplified one-dimensional case, where both the input x and the frequencies ω are treated as scalars. In this scalar context, a QFM is defined as a function returning the expectation value of some observable

$$f_\theta(x) = \langle 0 | U^\dagger(x, \boldsymbol{\theta}) M U(x, \boldsymbol{\theta}) | 0 \rangle \tag{2.29}$$

which can be interpreted as a truncated Fourier series:

$$f_\theta(x) = \sum_{\omega \in \Omega} c_\omega(\boldsymbol{\theta}) e^{i\omega x}. \tag{2.30}$$

The quantum circuit architecture in the function is given by

$$U(x;\boldsymbol{\theta}) = W^{(L+1)}(\boldsymbol{\theta}) S(x) W^{(L)}(\boldsymbol{\theta}) \cdots W^{(2)}(\boldsymbol{\theta}) S(x) W^{(1)}(\boldsymbol{\theta}). \tag{2.31}$$

Where the data encoding circuit, consisting of $S(x)$, utilizing single-qubit Pauli rotations, determines the accessible frequencies Ω (with r sequential or parallel encodings allowing access to r frequencies), while the trainable parameters $\boldsymbol{\theta}$ determine the coefficients c_ω.

3. Related Work

This work can be seen under two different perspectives. On the one hand this work can be motivated by noise in the NISQ era, which makes error mitigation a necessary technique to improve performance. To then analyze the performance, mathematical properties of the quantum circuits are investigated, such as Fourier analysis within the research area of QFM. In this case the use of pulse-level modeling provides a more detailed framework which could allow to better analyze the different types of noise and its influence on the performance. The other motivation is to measure and enhance the capabilities of quantum circuits, which is important for choosing effective circuits that ideally represent the solution space while maintaining low circuit depth and parameter count. Therefore, measures like expressibility and entangling capability are analyzed [124]. Such metrics are important as well to analyze quantum advantage [110]. In this context, pulse-level modeling, due to its high control, could open the doors for a new perspective on these metrics and possibly enhance them more. This is regarded mainly under the aspect of learning the pulse parameters, under a given goal to maximize one of these metrics. In the following sections, current research related to these two motivations is reflected upon: noise in Section 3.1, quantum Fourier analysis in Section 3.2, and pulse optimization in Section 3.3.

3.1. Noisy Intermediate-Scale Quantum Era

The current era of quantum computing is often referred to as the Noisy Intermediate Scale Quantum (NISQ) era. This term describes quantum processors that have a moderate number of qubits (typically tens to hundreds) but suffer from significant levels of noise [66]. Noise in these processors only enables an approximation to ideal quantum computation. Common errors caused by noise include leakage (qubit transitions out of the defined space used for computation), SPAM (imperfections in state preparation and measurement) [60], decoherent noise (loss of superposition and entanglement, including decoherence and dissipation), and coherent noise, which introduces systematic inaccuracies in quantum operations [134]. The challenges posed by noise in NISQ processors necessitate dedicated research efforts focused on understanding, characterizing, and ultimately mitigating its detrimental effects on quantum computations. Building upon the understanding of noise characteristics, researchers have explored methods to quantify the impact of noise on quantum information processing capabilities. For instance, [135] introduced a novel hybrid quantum-classical approach to estimate quantum channel capacities, which indicates how much information can be reliably sent through a quantum channel. This method combines

the variational quantum eigensolver algorithm with classical optimization techniques to compute these capacities.

Further exploring the landscape of noise in quantum circuits, investigations have also focused on developing efficient classical methods to simulate and analyze the behavior of noisy quantum systems. [40] constructed a classical simulation algorithm named *LOWESA*, which is designed to estimate expectation values of noisy parameterized quantum circuits. Under specific conditions on the circuits and with certain assumptions about the noise, *LOWESA* is shown to provide an efficient, polynomial algorithm in terms of the number of qubits and depth. The approximation error decreases exponentially with the physical error rate and a controllable cut-off parameter.

The insights gained from analyzing and simulating noise, as investigated by Fontana et al. [41], pave the way for practical strategies to reduce its impact on quantum computation. Their work specifically examines the effects of noise on parameterized quantum circuits through spectral analysis, utilizing signal processing tools to identify and remove noise-induced frequencies in the output of quantum circuits. They demonstrate that filtering these noise-induced modes effectively mitigates device errors, highlighting the increasing importance of characterizing and verifying quantum computations for NISQ applications.

Indeed, despite the inherent limitations of noisy hardware, significant progress is being made in developing error mitigation techniques to enhance the accuracy of quantum computations on current quantum devices. As shown by small-scale experimental demonstrations, approximations can be vastly improved by error mitigation in the computation of expectation values, enhanced by additional error suppression techniques and native gate decomposition, which reduce the circuit time [61].

3.2. Quantum Fourier Models

The work by [119] offers an interpretation of variational quantum circuits as partial Fourier series. The study highlights that the frequencies within these series are determined by the data-encoding Hamiltonians employed, while the coefficients are influenced by the design of the quantum circuit itself. Repeating encoding gates, such as Pauli rotations, enriches the frequency spectrum, thereby increasing the model's expressivity, or ability to represent complex functions. Notably, the authors provide a proof demonstrating that with sufficiently flexible trainable blocks, quantum models can asymptotically approximate any function, establishing their capability as universal function approximators [119]. Notably, this idea closely relates to the data re-uploading method introduced by [91] preceding Schuld's publication, and will be discussed in the following as a key technique.

3.2.1. Architectures

To improve model capabilities and address limitations, the research discussed in this subsection explores new techniques in data encoding, circuit design, and parameter training.

One such technique, focusing on circuit design for enhanced classification, is the use of data re-uploading. A universal quantum classifier, as detailed in [91], utilizes data re-uploading. This approach demonstrates that a single qubit, integrated with a classical subroutine and repeated data re-uploading, can achieve universal quantum classification. The capacity to re-upload data multiple times is crucial for surpassing the inherent constraints of a single qubit. The quantum circuits for this type of classifier are structured with sequential units that perform data re-uploading and single-qubit processing. Through data re-uploading and measurements, the classifier can manage multiple input dimensions and output categories, enabling universal classification. The efficiency of this classification strategy can be further improved by incorporating multiple qubits and entanglement. The referenced paper also presents benchmarking results for single-qubit classifiers.

Another area of investigation centers on optimizing data encoding strategies. Drawing on the no-cloning principle [132], the research explores the potential benefits of encoding the input redundantly. This paper establishes lower bounds on the required number of redundant input copies to enable a PQC's expectation value function to accurately match a specific target function.

Beyond data handling, advancements in parameter training are also being explored. In *Let Quantum Neural Networks Choose Their Own Frequencies* [54], a generalization of quantum machine learning models termed trainable-frequency (TF) quantum models is presented. Traditional quantum models typically have fixed frequencies in their partial Fourier series representation, determined by the generator Hamiltonians of the selected feature map. In contrast, TF models incorporate trainable parameters within the generator, enabling the model to learn its own optimal frequencies. Numerical experiments conducted in the paper illustrate that TF models can learn generators exhibiting advantageous characteristics, including non-regularly spaced frequencies and adaptable spectral richness.

3.2.2. Metrics and Limitations

Quantum Fourier models are also employed in the context of classical approximations of quantum machine learning. Researchers [65] have developed a classical sampling technique based on random Fourier features to approximate quantum feature maps using classical computation. The authors provide theoretical guarantees on the number of frequency samples needed to accurately approximate models with large quantum feature spaces, demonstrating that this number scales favorably with the size of the quantum spectrum. This finding suggests that for specific PQC, the potential for a "quantum advantage" in machine learning tasks may be limited, as classical models could achieve comparable predictive performance.

A key challenge with circuit depth is that more expressive circuits, like 2-designs, often become harder to train. This is due to the phenomenon of Barren plateau, where the gradients of the loss function become exponentially small as the circuit depth increases [105]. Therefore research focuses on introducing metrics to efficiently categorize quantum models and like this optimize their architecture design.

Choosing the right quantum model for a given task remains a significant challenge in quantum machine learning. The research discussed in the following offers insights into addressing this. It explores the use of Fourier analysis for circuit characterization and prediction, introduces methods for circuit selection based on expressibility and entanglement and reveals limitations of quantum models.

A recent study [139] builds upon prior work [119] by examining the function space of PQC through the lens of Fourier analysis, describing it as a truncated Fourier sum. The research highlights that while the encoding gates of a PQC influence the spectrum of this sum, the variational components can actively suppress certain frequency coefficients, effectively removing them from the spectrum. Notably, this paper provides the first detailed characterization of how these Fourier coefficients depend on the variational parameters, demonstrating that they are trigonometric polynomials. Furthermore, the authors introduce an algorithm capable of precisely calculating the spectrum and corresponding Fourier coefficients for any given quantum circuit. The study suggests that by comparing the Fourier transform of a dataset with the accessible spectra of various PQC, it becomes possible to predict which PQC architecture would be most suitable for fitting the data.

A key challenge in utilizing PQC lies in choosing an effective circuit design that achieves a balance between its ability to represent complex functions and practical constraints such as circuit depth and the number of adjustable parameters. To address this, researchers [124] have introduced several statistically estimated descriptors, with a particular focus on measures of expressibility and entangling capability, which is shown to be related to expressibility. These metrics are proposed as tools for characterizing and identifying PQC that are both powerful and compact. The study presents a variety of circuit architectures and visualizes their corresponding metric values.

Further investigation into the representational capabilities of quantum models has revealed new insights into the relationship between a model's Fourier coefficients and its encoding gates [83]. A central idea in this work is the concept of frequency redundancy within the Fourier series spectrum and its impact on the spectrum's significance. Mhiri et al. identify a "vanishing expressivity" phenomenon that can occur under certain conditions, where specific Fourier coefficients diminish exponentially with an increasing number of qubits. These observations point to new constraints that limit the representational power of PQC, suggesting a new inherent bias in quantum models.

3.3. Pulse Level Modeling

Quantum computing at the pulse-level involves using precise microwave or laser pulses to control quantum systems, enabling operations like quantum gates. This approach is crucial for advancing quantum technology, offering richer controllability by varying the Hamiltonian to achieve desired states. However, it faces challenges such as accurately modeling the machine Hamiltonian, which can drift and requires daily recalibration.

Despite the potential advantages discussed in Section 2.2, several notable challenges are associated with pulse-level control. A primary difficulty lies in the necessity for precise system modeling, a process that can be intricate and time-consuming. Furthermore, the pulse-level programming approach demands a thorough understanding of the underlying quantum hardware. Even minor inaccuracies in the system model can introduce errors into the quantum operations [126]. Moreover, as highlighted by Magann et al. [77], the effective implementation of optimal control within Variational Quantum Pulses (VQPs) necessitates sufficient control resources. Without these resources, the potential benefits offered by pulse-level control may be limited.

Addressing these complexities, the field of pulse optimization seeks to develop methodologies for effectively designing and implementing these intricate control sequences. This effort is largely driven by Quantum Optimal Control (QOC), which, rooted in classical mechanics, focuses on designing electromagnetic fields for the manipulation of quantum systems [6]. Numerical algorithms are indispensable for solving these QOC problems.

A variety of algorithms have emerged to tackle quantum optimal control, each with its own strengths and applications. One prominent method is Gradient Ascent Pulse Engineering (GRAPE). Introduced by de Fouquieres et al. [43], GRAPE optimizes objective functions in open quantum systems by calculating the gradient for general N-level open quantum systems, specifically considering piecewise control. This algorithm iteratively refines control pulses through gradient ascent, making it a popular choice for applications such as state engineering in superconducting circuits and ion traps [75], as well as for optimizing coherence and decoherence [92].

Building on the concept of robust control, Dong et al. [35] introduced a sampling-based learning method designed to discover robust control pulses for generating universal quantum gates. Their numerical results demonstrate that the learned robust control fields are unaffected by disturbances, uncertainties, and fluctuations during the creation of these gates. This learning control method effectively identifies optimal control fields, and the resulting quantum gates exhibit enhanced robustness and reliability against various fluctuations and uncertainties.

Another notable algorithm is Chopped RAndom Basis (CRAB), developed by Caneva et al. [18]. CRAB efficiently optimizes quantum processes, achieving results comparable to other methods but with significantly less resource usage. Its versatility lies in its ability to construct pulses and handle various objectives and constraints.

More recently, the concept of quantum pulse learning has emerged, as explored by Liang et al. [70]. This method optimizes parametrized pulse characteristics for desired operations, showcasing advantages in expressivity, entanglement capability, and efficiency. Its practical benefits have been demonstrated through improvements in quantum chemistry and finance applications.

4. Methodology

This chapter's primary focus is the theoretical derivation demonstrating the equivalence defined in Equation 1.2. Building upon the concepts from Subsection 2.1.1 of the preliminary chapter, the solution to the Schrödinger equation, derived in Section 4.1, and unitary transformations, developed in Section 4.3, provide the foundation for constructing the Hamiltonians essential to the pulse-level framework $f'_{\theta,\Pi}$. These Hamiltonians are elaborated upon in Sections 4.2, 4.4, 4.5, and 4.6. Metrics used to numerically validate and quantifying deviations are presented in Section 4.7. Furthermore, the Fourier analysis groundwork established in Section 2.3 is employed to define the Fourier characteristics necessary for comparing gate and pulse-based evaluations, as presented in Section 4.8.

4.1. Solving the Schrödinger Equation

To derive a pulse-level description of a quantum gate, the task is to find a Hamiltonian $\hat{H}$ whose time evolution generates the gate's unitary operator $\hat{U}$ [69]. This is achieved by solving Schrödinger Equation 2.2, with $\hbar = 1$

$$\frac{d}{dt}|\Psi(t)\rangle = -i\hat{H}|\Psi(t)\rangle \tag{4.1}$$

For a bounded time-independent operator, the solution is given by a unitary evolution operator $\hat{U}(t, t_0)$[85]

$$|\Psi(t)\rangle = \hat{U}(t, t_0)|\Psi(t_0)\rangle \tag{4.2}$$

$$\hat{U}(t, t_0) = e^{-i\int_{t_0}^{t} dt'\hat{H}} \tag{4.3}$$

However, when the Hamiltonian is time-dependent, its eigenstates evolve with time. This means that the basis of states that diagonalizes the Hamiltonian is not constant, making it significantly more complex to solve the Schrödinger equation as a fixed basis cannot be used throughout the evolution [85].

$$\hat{U}(t, t_0) = \hat{T}e^{-i\int_{t_0}^{t} dt'\hat{H}(t')} \tag{4.4}$$

This can then be solved using the time-ordering operator $\hat{T}$, which expands into the Dyson series [37] to solve the equation [85].

To design control pulses the Hamiltonian can be formulated as a linear composition consisting of a static and a time-dependent part [71]:

$$H(t) = \underbrace{H_0}_{\substack{\text{static} \\ \text{Hamiltonian}}} + \sum_j \underbrace{S_j(t)}_{\substack{\text{Hamiltonian} \\ \text{signals}}} \underbrace{H_j}_{\substack{\text{Hamiltonian} \\ \text{operators}}} \tag{4.5}$$

To avoid confusion with the term "drive" Hamiltonian, the static Hamiltonian is also known as the drift Hamiltonian [145] and will not be referred to as such in this context. With the Hamiltonian structured to account for both static and time-dependent elements, the next step is to examine the static Hamiltonian in detail.

4.2. Static Hamiltonian

A static Hamiltonian is, by definition, a time-independent Hamiltonian. In the absence of external driving forces, a static Hamiltonian describes a system where energy is conserved. Consequently, for a system solely governed by such a Hamiltonian, there are no changes in measurements or observables over time.

For a closed two-level system, energy is quantized, meaning it possesses two discrete eigenvalues associated with its two states. As discussed in Section 2.2, the Bohr frequency condition states:

$$\Delta E = E_1 - E_0 = \hbar\omega_q \tag{4.6}$$

where $\hbar$ is the reduced Planck constant and ω_q is the transition frequency between the two levels.

It's common and convenient to choose the zero point of energy to be halfway between the two energy states. With this convention, the energy eigenvalues are often set as $E_1 = +\frac{\hbar\omega_q}{2}$ for the excited state $|1\rangle$ and $E_0 = -\frac{\hbar\omega_q}{2}$ for the ground state $|0\rangle$.

Through spectral decomposition (as shown in Equation 2.6), the static Hamiltonian can be written as $H_{\text{static}} = E_0|0\rangle\langle 0| + E_1|1\rangle\langle 1|$. Subsequently, substituting the eigenvalues, as detailed in [143] $H_{\text{static}} = \frac{\hbar\omega_q}{2}|1\rangle\langle 1| - \frac{\hbar\omega_q}{2}|0\rangle\langle 0|$. This Hamiltonian can also be expressed using the Pauli Z matrix, σ_z, yielding $H_{\text{static}} = -\frac{\hbar\omega_q}{2}\sigma_z$

Nevertheless, even though this is the most common form of defining an unperturbed Hamiltonian [17, 140, 143], it is important to note that there is no fundamental physical law dictating this specific assignment of eigenvalues. It is also entirely possible to choose the eigenvalues the other way around, and indeed, conventions often differ within the scientific literature. For example, with the opposite sign convention for σ_z in the Hamiltonian, one might find $H_{\text{static}} = \frac{\hbar\omega_q}{2}\sigma_z$ as presented in [26, 14]. It is also worth noting that the static Hamiltonian is inherently Hermitian, which can be demonstrated as follows:

$$H_{\text{static}}^\dagger = \left(\frac{\omega_q}{2}\sigma_z\right)^\dagger = \left(\frac{\omega_q}{2}\right)^* \sigma_z^\dagger = \frac{\omega_q}{2}\sigma_z = H_{\text{static}} \tag{4.7}$$

The key is to be consistent with the chosen convention throughout any given analysis. In the following this definition $H_{\text{static}} = \frac{\hbar\omega_q}{2}\sigma_z$ of the static Hamiltonian is used.

4.3. Rotating frame

A unitary transformation can be expressed in terms of the time-dependent Hamiltonian $H(t)$ and unitary operator $U(t)$, as detailed in Subsection 2.1.1. Under this change, the Hamiltonian in the laboratory frame $H_{\text{lab}}(t)$ transforms to the Hamiltonian in the rotating frame $H_{\text{rot}}(t)$ as:

$$H_{\text{rot}}(t) = U^{\dagger}(t)H_{\text{lab}}(t)U(t) - i\hbar U^{\dagger}(t)\frac{dU(t)}{dt} \tag{4.8}$$

and the states transforms as:

$$|\psi_{\text{rot}}(t)\rangle = U^{\dagger}(t)|\psi_{\text{lab}}(t)\rangle. \tag{4.9}$$

A specific case of the unitary transformation is the rotating frame transformation, which is a widely used technique in quantum optics, particularly for solving two-level and three-level systems [142]. It is defined by the unitary transformation $U(t) = e^{-iH_{\text{static}}t/\hbar}$ and will be used for the following pulses. In the following equation, the influence on the term $-i\hbar U^{\dagger}(t)\frac{dU(t)}{dt}$ is shown:

$$\begin{aligned}
-i\hbar U^{\dagger}(t)\frac{dU(t)}{dt} &\underset{(1)}{=} -i\hbar\left(e^{-iH_{\text{static}}t/\hbar}\right)^{\dagger}\frac{d}{dt}\left(e^{-iH_{\text{static}}t/\hbar}\right)\\
&\underset{(2)}{=} -i\hbar e^{iH_{\text{static}}t/\hbar}\frac{d}{dt}\left(e^{-iH_{\text{static}}t/\hbar}\right)\\
&\underset{(3)}{=} -i\hbar e^{iH_{\text{static}}t/\hbar}\left(\frac{-i}{\hbar}H_{\text{static}}e^{-iH_{\text{static}}t/\hbar}\right)\\
&\underset{(4)}{=} -e^{iH_{\text{static}}t/\hbar}H_{\text{static}}e^{-iH_{\text{static}}t/\hbar}\\
&\underset{(5)}{=} -H_{\text{static}}e^{iH_{\text{static}}t/\hbar}e^{-iH_{\text{static}}t/\hbar}\\
&\underset{(6)}{=} -H_{\text{static}}e^{(iH_{\text{static}}t/\hbar)-(iH_{\text{static}}t/\hbar)}\\
&\underset{(7)}{=} -H_{\text{static}}
\end{aligned}$$

Here are the detailed explanations for each step in the derivation: (1) simplifies; (2) since H_{static} is Hermitian (Subsection 4.2) (3) using the chain rule for operator exponentials, $\frac{d}{dt}f(t)A = \frac{df(t)}{dt}A, \quad$ given that $[A, f(t)A] = 0$[112], which is true here since $A =$

$-iH_{\text{static}}/\hbar$ is time-independent. Thus, $\frac{d}{dt}\left(e^{-iH_{\text{static}}t/\hbar}\right) = \left(\frac{-iH_{\text{static}}}{\hbar}\right)e^{-iH_{\text{static}}t/\hbar}$; (4) simplifies; (5) $H_{\text{static}}e^{-iH_{\text{static}}t/\hbar} = e^{-iH_{\text{static}}t/\hbar}H_{\text{static}}$, since H_{static} commutes with $e^{-iH_{\text{static}}t/\hbar}$; (6) since H_{static} commutes with itself $e^{A+B} = e^Ae^Be^{-\frac{1}{2}[A,B]} = e^Ae^B \quad \text{if } [A,B] = 0$ [44]; (7) simplifies

Substituting it back to Equation 4.8 and using that $e^{iH_{\text{static}}t/\hbar}H_{\text{static}}e^{-iH_{\text{static}}t/\hbar} = H_{\text{static}}$, the equation further simplifies to

$$\begin{aligned} H_{\text{rot}} &= e^{iH_{\text{static}}t/\hbar}(H_{\text{static}} + H_{\text{drive}}(t))e^{-iH_{\text{static}}t/\hbar} - H_{\text{static}} \\ &= e^{iH_{\text{static}}t/\hbar}H_{\text{static}}e^{-iH_{\text{static}}t/\hbar} + e^{iH_{\text{static}}t/\hbar}H_{\text{drive}}(t)e^{-iH_{\text{static}}t/\hbar} - H_{\text{static}} \\ &= H_{\text{static}} + e^{iH_{\text{static}}t/\hbar}H_{\text{drive}}(t)e^{-iH_{\text{static}}t/\hbar} - H_{\text{static}} \\ &= e^{iH_{\text{static}}t/\hbar}H_{\text{drive}}(t)e^{-iH_{\text{static}}t/\hbar} \end{aligned}$$

Substituting H_{static} for the two-level Hamiltonian from Subsection 4.2 , the resulting Hamiltonian becomes

$$H_{\text{rot}}(t) = e^{i\frac{\omega_q}{2}\sigma_z}H_{\text{drive}}(t)e^{-i\frac{\omega_q}{2}\sigma_z} = H_{\text{eff}}(t) \tag{4.10}$$

and will be used henceforth. Literature often refers to H_{rot} as the effective Hamiltonian H_{eff}.

4.4. Drive Hamiltonians

To effectively control and manipulate a qubit's quantum state, this section focuses on the drive Hamiltonians for single-qubit gates, outlining the specific single-qubit gates necessary for the pulse-level framework: X and Y rotation are covered in Subsection 4.4.1, while the Z rotation is detailed Subsection 4.4.2. Subsection 4.4.3 presents the pulse-level Hadamard gate, which incorporates a global phase correction further discussed in Subsection 4.4.4. The drive Hamiltonians are central to controlling a quantum system's evolution describing how external control fields interact with the qubits. These external fields are considered external degrees of freedom operating within the otherwise closed quantum system.

For time-independent Hamiltonians, a standard pulse duration of $T = 12$ ns is used universally, as in [3]. Generally, when performing numerical simulations, the choice of discrete time step length presents a trade-off: finer time steps yield more accurate results, but at the expense of increased computational resources [26].

4.4.1. X, Y - Rotations

X and Y rotations drive transitions between the ground and excited states of a qubit. While the following discussion primarily uses the σ_x operator, the described pulse schemes are equally applicable to σ_y.

A common approach for inducing these transitions involves Gaussian or Gaussian-like modulated pulses with a sinusoidal carrier frequency [140, 17]. On practical quantum hardware, Derivative Removal by Adiabatic Gate (DRAG) pulses are frequently employed for modulation to enhance the suppression of leakage to unwanted energy levels [50, 138].

The Gaussian pulse envelope is mathematically defined as:

$$f(t, \mu, \sigma) = A \cdot \exp\left(-\frac{(t - \frac{T}{2})^2}{2\sigma^2}\right) \tag{4.11}$$

where A is the amplitude, $\mu = \frac{T}{2}$ represents the center of the pulse, and σ is the standard deviation determining the pulse width. This envelope is then modulated by a sinusoidal carrier wave, $x'(t) = \sin(\omega_c t + \phi_c)$., where ω_c is the carrier frequency in radians per second and ϕ_c is the carrier phase.

The resulting time-dependent control signal, $S'(t) = f(t; \mu, \sigma)x'(t)$ with $|S'(t)| \leq 1$, drives the qubit according to the Hamiltonian [140] [17]:

$$H_{\text{drive}}(t) = \Omega S'(t)\sigma_x \tag{4.12}$$

scaled by Rabi frequency Ω. It's worth noting that equivalent qubit rotations can be achieved using alternative carrier wave functions, such as a cosine. As will be shown, a cosine carrier can offer certain advantages.

In the following the control signal from [23] will be used:

$$S(t) = \text{Re}\left[f(t)e^{i\omega_c t + \phi_c}\right] \tag{4.13}$$

which is equivalent to

$$S'(t) = f(t)\sin(\omega_c t + \phi_c) \tag{4.14}$$

as shown in the following: For $f(t) \in \mathbb{R}$

$$\begin{aligned} x(t) &= \text{Re}\left[e^{i\omega_c t + \phi_c}\right] \\ &= \text{Re}\left[\cos(\omega_c t + \phi_c) + i\sin(\omega_c t + \phi_c)\right] \\ &= \cos(\omega_c t + \phi_c) \\ &= \sin(\omega_c t + \phi_c') \quad \text{with } \phi_c' = \phi_c + \frac{\pi}{2} \\ &= x'(t) \end{aligned}$$

Furthermore, the complex exponential form offers a convenient interpretation. Setting the carrier frequency $\omega_c = 0$ and phase $\phi_c = 0$ simplifies the exponential to $e^0 = 1$, resulting in a control signal that directly follows the pulse envelope:

$$S(t) = f(t) \tag{4.15}$$

For a desired gate rotation angle θ, the tunable parameters for the pulse shaping are consistent with standards used by IBM authors [3, 128], with example values including an

amplitude $A = 1$, a standard deviation $\sigma = 15$, a carrier frequency $\omega_c = \omega_q = 10\pi$ rad/s, and a carrier phase $\phi_c = 0$. The Rabi frequency depends on the hardware and simulation used, and is approximately equal to the gate parameter $\Omega \approx \theta$. Since $x(t) = \text{Re}\left[e^{i\omega_c t + \phi_c}\right] = \cos(\omega_c t + \phi_c)$ will be used for the carrier frequency, the drive Hamiltonian with a cosine carrier wave can be expressed as $H_{\text{drive}}(t) = f(t, \mu, \sigma)\cos(\omega_c t + \phi_c)\Omega\sigma_x$.

4.4.2. Z Rotation

A rotation around the Z-axis does not alter probabilities and can be implemented using composite X and Y gates [80]. Here, the advantages of unitary transformations (see Section 4.3), particularly relevant for Z-axis rotations, are utilized.

The chosen envelope is constant, $f(t) = \Omega$, with no carrier-frequency ($\omega_c = 0.0$ phase = $\phi_c = 0.0$). This makes the control signal constant as a whole: $S(t) = \Omega\cos(\omega_c t + \phi_c) = \Omega\cos(0) = \Omega$

Consequently, the Hamiltonian operator becomes the drive Hamiltonian:

$$H_{\text{operator}} = \Omega\sigma_z = H_{\text{drive}}(t) = H_{\text{drive}} \tag{4.16}$$

When transformed into the rotating frame, the effective Hamiltonian becomes:

$$H_{\text{rot}} = e^{i\frac{\omega_q}{2}\sigma_z}\Omega\sigma_z e^{-i\frac{\omega_q}{2}\sigma_z} \tag{4.17}$$

This demonstrates that the effective Hamiltonian in the rotating frame is simply the drive Hamiltonian:

$$\begin{aligned}
H_{\text{rot}} &\underset{(1)}{=} \begin{pmatrix} e^{i\frac{\omega_q}{2}} & 0 \\ 0 & e^{-i\frac{\omega_q}{2}} \end{pmatrix} \Omega \begin{pmatrix} 1 & 0 \\ 0 & -1 \end{pmatrix} \begin{pmatrix} e^{-i\frac{\omega_q}{2}} & 0 \\ 0 & e^{i\frac{\omega_q}{2}} \end{pmatrix} \\
&= \Omega \begin{pmatrix} e^{i\frac{\omega_q}{2}} & 0 \\ 0 & -e^{-i\frac{\omega_q}{2}} \end{pmatrix} \begin{pmatrix} e^{-i\frac{\omega_q}{2}} & 0 \\ 0 & e^{i\frac{\omega_q}{2}} \end{pmatrix} \\
&= \Omega \begin{pmatrix} 1 & 0 \\ 0 & -1 \end{pmatrix} \\
&= \Omega\sigma_z \\
&= H_{\text{drive}}
\end{aligned}$$

Step (1) involves a power series expansion, as in Equation 2.15, with the subsequent steps being simplifications.

By setting the Rabi frequency in dependence of time $\Omega \approx \frac{\theta}{2}$, for every duration T the equivalence is shown:

$$U(T) = e^{-i\int_0^T dt' \hat{H}(t')} \underset{(1)}{=} e^{-i\hat{H}T} = e^{-i\left(\frac{\theta}{2}\sigma_z\right)T} = e^{-i\frac{\theta}{2}\sigma_z} \underset{(2)}{=} RZ(\theta) \tag{4.18}$$

This holds true (1) since the Hamiltonian is time-independent and (2) the power expansion of Pauli matrices is utilized (Equation 2.15).

4.4.3. Hadamard

The Hadamard gate operation can be achieved by shaping the pulse applied to the qubit. The drive Hamiltonian for this process can be constructed using the σ_x operator, as given by [35]: $H_{\text{total}}(t) = \Omega_0\sigma_z + \Omega_x(t)\sigma_x$.

For this framework, the Hadamard gate is implemented using three pulses, with the first pulse being the primary pulse. Following the methodology from [35] the σ_x operator is incorporated in the Hamiltonian operator as well, specifically for the applied pulse:

$$H_{\text{drive}}(t) = f(t;\mu,\sigma)\cos(\omega_c t + \phi_c)\Omega\sigma_x \tag{4.19}$$

Here $f(t;\mu,\sigma)$ represents a Gaussian pulse shape:

$$f(t;\mu,\sigma) = A \cdot \exp\left(-\frac{(t - T/2)^2}{2\sigma^2}\right) \tag{4.20}$$

and the core Hamiltonian operator for the pulse:

$$H_{\text{operator}} = \Omega\sigma_x \tag{4.21}$$

For this implementation, the pulse is characterized by a duration $T = 12ns$, a Gaussian standard deviation $\sigma = 15$, and a Gaussian amplitude $A = 1$. The carrier and qubit frequencies are set to $\omega_c = \omega_q = 10\pi$ rad/s with a carrier phase $\phi_c = -\pi/2$, while the Rabi frequency Ω depends on the specific hardware. Transforming to the rotating frame with respect to the qubit frequency ω_q, the effective Hamiltonian becomes:

$$H_{\text{eff}}(t) = e^{i\frac{\omega q}{2}\sigma_z} f(t;\mu,\sigma)\cos(\omega_c t + \phi_c)\Omega\sigma_x e^{-i\frac{\omega q}{2}\sigma_z} \tag{4.22}$$

The time evolution of the quantum state under this Hamiltonian can be solved using the Dyson series,

$$\hat{U}(t,t_0) = \hat{T}e^{-i\int_{t_0}^{t} dt' e^{i\frac{\omega q}{2}\sigma_z} f(t';\mu,\sigma)\cos(\omega_c t' + \phi_c)\Omega\sigma_x e^{-i\frac{\omega q}{2}\sigma_z}}, \tag{4.23}$$

which uses the time ordering operator $\hat{T}$ which is defined as

$$\hat{T}[\hat{H}(t')\hat{H}(t)] \equiv \Theta(t' - t)\hat{H}(t')\hat{H}(t) + \Theta(t - t')\hat{H}(t)\hat{H}(t') \tag{4.24}$$

with $\Theta(t' - t)$ denoting the Heaviside theta function [85].

For the second pulse a Z-rotation is applied as in section 4.4.2. For numerical tests, this leads to the correct quantum states (fidelity) but not the same global phase factor, which will be explained more in section 4.7. Therefore, a third pulse is used to correct the global phase. This is discussed in the following subsection.

4.4.4. Global Phase Factor

Let n be the number of parallel applied Hadamard pulses in a multi state system following the structure as in subsection 4.5.2

After numerical tests the following global phase error compared to the desired state was observed:

$$\gamma_{\text{error}} = \begin{cases} -\frac{\pi}{2} & \text{if } n \equiv 1 \pmod 4 \\ -\pi & \text{if } n \equiv 2 \pmod 4 \\ \frac{\pi}{2} & \text{if } n \equiv 3 \pmod 4 \\ 0 & \text{if } n \equiv 0 \pmod 4 \end{cases} \tag{4.25}$$

To obtain the correct global phase factor, a correction angle $\gamma_{\text{correction}} = -\gamma_{\text{error}}$ is needed for a correct global phase factor.

$$\gamma_{\text{correction}} = \begin{cases} \frac{\pi}{2} & \text{if } n \equiv 1 \pmod 4 \\ \pi & \text{if } n \equiv 2 \pmod 4 \\ -\frac{\pi}{2} & \text{if } n \equiv 3 \pmod 4 \\ 0 & \text{if } n \equiv 0 \pmod 4 \end{cases} \tag{4.26}$$

On the complex plane, the accumulation of errors becomes visually apparent. Each subsequent Hadamard pulse introduces a $-\frac{\pi}{2}$ or clockwise rotation. Therefore, the error correction process necessitates an opposite, counter-clockwise rotation. Notably, when the total count of Hadamard pulses is a multiple of four, the net global phase error is zero and no correction is needed.

To apply specific energies, a time-independent Hamiltonian may be defined. The tunable parameters are established as a constant envelope $f(t) = 1.0$ and an absence of oscillation such that $x(t) = \cos(\omega_c t + \phi_c) = cos(0) = 1$. Consequently, the resulting modulation is $S(t) = f(t)x(t) = 1.0$. Utilizing the solution of the time-independent Schrödinger equation, $|\psi(t)\rangle = e^{-iHt/\hbar}|\psi(0)\rangle$, and considering the application of a global phase factor $e^{i\gamma_{\text{correction}}}$, the following relation holds: $e^{-iHt}|\psi(0)\rangle = e^{i\gamma_{\text{correction}}}|\psi(0)\rangle$. From this, the Hamiltonian is defined as $H = -\gamma_{\text{correction}}\mathbb{I}$. Analogous to the Z-Rotation (Subsection 4.4.2), the effective Hamiltonian is identical to the drive Hamiltonian in this context, such that $H_{\text{drive}}(t) = H_{\text{eff}}(t) = H_{\text{eff}}$. Thus for $T = 1$ and $\hbar = 1$, the unitary operator becomes $U(T) = e^{-iH_{\text{eff}}T/\hbar} = e^{-i(-\gamma_{\text{correction}}\mathbb{I})T/\hbar} = e^{i\gamma_{\text{correction}}T/\hbar}I = e^{i\gamma_{\text{correction}}}I$, which is equivalent to applying a global phase factor.

4.5. Hamiltonians for Multiple States

When composing circuits of multiple qubits it is necessary to define how the system's Hamiltonian, and consequently its time evolution, are constructed from the individual qubit Hamiltonians. This section details the two main principles governing this construction.

4.5.1. Single-Qubit Hamiltonian

When a Hamiltonian acts non-trivially on only one qubit within a multi-state system, the time evolution operator for the entire system can be expressed as a tensor product where the time evolution operator for that specific qubit is tensored with identity operators for all other qubits $\hat{H}_{\text{total}} = I \otimes \cdots \otimes \hat{H}_i \otimes \cdots \otimes I$.

$$
\begin{aligned}
U(t)_{\text{total}} &\underset{(1)}{=} e^{-i\hat{H}_{\text{total}}t/\hbar} \\
&\underset{(2)}{=} e^{-i(I\otimes\cdots\otimes\hat{H}_i\otimes\cdots\otimes I)t/\hbar} \\
&\underset{(3)}{=} e^{(I\otimes\cdots\otimes(-\frac{it}{\hbar}\hat{H}_i)\otimes\cdots\otimes I)} \\
&\underset{(4)}{=} I \otimes \cdots \otimes e^{-i\hat{H}_i t/\hbar} \otimes \cdots \otimes I \\
&\underset{(5)}{=} I \otimes \cdots \otimes U_i(t) \otimes \cdots \otimes I
\end{aligned}
$$

The transformation steps are explained as follows: (1) epresents a general simplification of the time evolution operator; (2) involves substituting the defined total Hamiltonian into the exponential; (3) scalar multiplication is applied within the exponential, associating the scalar factor $-it/\hbar$ with the Hamiltonian operator $\hat{H}_i$ within the tensor product, which is a property of scalar multiplication with tensor products: $c(A \otimes B) = (cA) \otimes B = A \otimes (cB)$ [46]; (4) utilizes the property of the exponential of a tensor product with identity, where $e^{A\otimes I} = e^A \otimes I$ and $e^{I\otimes B} = I \otimes e^B$, similar to the simplification of the power series in Subsection 2.1.3.1 [11]; (5) represents the definition of the time evolution operator for the i-th individual qubit, where $U_i(t) = e^{-iH_i t/\hbar}$ denotes the time evolution of this qubit under its local Hamiltonian H_i.

4.5.2. Independent Single-Qubit Hamiltonians

For a system of non-interacting qubits, where each qubit possesses its own independent Hamiltonian, the total Hamiltonian is expressed as the sum of these individual Hamiltonians, with each tensored with identities on the other qubits, as noted by [39]. This leads to $\hat{H}_{\text{total}} = \hat{H}_1 + \hat{H}_2 + \cdots + \hat{H}_n = \sum_{i=1}^{n} \hat{H}_i$. The resulting time evolution operator for the entire system then factorizes into the tensor product of the time evolution operators for each individual qubit.

Consider a comprehensive example of applying a single-qubit gate to all qubits within such a multi-state system. The individual time evolution operators are:

$$e^{-iH_1^{(1)}t/\hbar} = e^{-i(H_1\otimes I\otimes\cdots)t/\hbar} = e^{-iH_1 t/\hbar} \otimes I \otimes \cdots \otimes I \tag{4.27}$$

$$e^{-iH_2^{(2)}t/\hbar} = e^{-i(I\otimes H_2\otimes\cdots)t/\hbar} = I \otimes e^{-iH_2 t/\hbar} \otimes \cdots \otimes I \tag{4.28}$$

$$\vdots$$

$$e^{-iH_n^{(n)}t/\hbar} = e^{-i(I\otimes I\otimes\cdots\otimes H_n)t/\hbar} = I\otimes I\otimes\cdots\otimes e^{-iH_nt/\hbar} \tag{4.29}$$

The total time evolution operator, $U(t)_{\text{total}}$, is derived through the following steps:

$$\begin{aligned} U(t)_{\text{total}} &= e^{-i\hat{H}_{\text{total}}t/\hbar} \\ &\underset{1.}{=} e^{-i\sum_{j=1}^{n} H_j^{(j)}t/\hbar} \\ &\underset{2.}{=} e^{-iH_1t/\hbar}\otimes e^{-iH_2t/\hbar}\otimes\cdots\otimes e^{-iH_nt/\hbar} \\ &\underset{3.}{=} U_1(t)\otimes U_2(t)\otimes\cdots\otimes U_n(t) \end{aligned}$$

For the first step (1) the total Hamiltonian is substituted, with each H_j representing the Hamiltonian operator acting solely on the j-th qubit in its local Hilbert space. Step (2) leverages the property of the exponential of the sum of commuting operators [39], which holds because the Hamiltonians of different, non-interacting subsystems commute; specifically, If $i \neq j,$ then $[H_i^{(i)}, H_j^{(j)}] = 0$. When operators commute, the exponential of their sum is equal to the product of their individual exponentials: $e^{A+B} = e^Ae^Be^{-\frac{1}{2}[A,B]} = e^Ae^B$ if $[A,B] = 0$ [44]. Finally, step (3) represents the tensor product of individual time evolution operators, defining $U_j(t) = e^{-iH_jt/\hbar}$ as the time evolution of each qubit under its local Hamiltonian H_j.

4.6. Controlled NOT - A Two-Qubit Operator

On the pulse-level, the Controlled-NOT (CNOT) gate is typically implemented using cross-resonance pulses [59]. At the hardware level, advanced techniques such as echoed pulse sequences are employed to enhance fidelities and mitigate errors [68]. By utilizing pulses that perform the logical Hadamard from Subsection 4.4.3) and introducing the Controlled-Z (CZ) gate in the following, the CNOT operation can be modeled with pulses analogous to its classical logical composition [48]:

$$\text{CNOT} = (I\otimes H)\text{CZ}(I\otimes H) \tag{4.30}$$

The CZ gate applies a phase of -1 only when both the control and the target qubits are in the $|1\rangle$ state. It's important to note, that the CZ gate is commutative, meaning CZ(0,1) = CZ(1,0) a property that will become apparent later. For clarity, however, the control qubit will hereafter be denoted by index i and the target qubit by index j, with the condition that $i \neq j$.

The matrix representation of the CZ gate is:

$$CZ = \begin{bmatrix} 1 & 0 & 0 & 0 \\ 0 & 1 & 0 & 0 \\ 0 & 0 & 1 & 0 \\ 0 & 0 & 0 & -1 \end{bmatrix} \tag{4.31}$$

For a n-qubit system, considering two qubits with indices i and j, their standard basis states are:

$$
\begin{aligned}
|00\rangle_{ij} &= |0\rangle_i \otimes |0\rangle_j \\
|01\rangle_{ij} &= |0\rangle_i \otimes |1\rangle_j \\
|10\rangle_{ij} &= |1\rangle_i \otimes |0\rangle_j \\
|11\rangle_{ij} &= |1\rangle_i \otimes |1\rangle_j
\end{aligned}
$$

Since the CZ operator causes a phase shift when both control and target qubits are in the $|1\rangle$ state and acts as the identity for all other qubits, its eigenvalues corresponding to these basis states are 1 and -1.

$$
\begin{aligned}
|00\rangle_{ij} &= 1|00\rangle_{ij} \\
|01\rangle_{ij} &= 1|01\rangle_{ij} \\
|10\rangle_{ij} &= 1|10\rangle_{ij} \\
|11\rangle_{ij} &= -1|11\rangle_{ij}
\end{aligned}
$$

The CZ operator can be rewritten using its spectral decomposition:

$$
\mathrm{CZ}_{ij} = (+1)|00\rangle_{ij}\langle 00|_{ij} + (+1)|01\rangle_{ij}\langle 01|_{ij} + (+1)|10\rangle_{ij}\langle 10|_{ij} + (-1)|11\rangle_{ij}\langle 11|_{ij}
$$

Considering an Hamiltonian with the same basis states $|00\rangle, |01\rangle, |10\rangle, |11\rangle$ and respective eigenvalues $E_{00}, E_{01}, E_{10}, E_{11}$, the CZ operator can also be expressed as the time evolution operator $U(T) = e^{-iHT}$:

$$
\begin{aligned}
\mathrm{CZ}_{ij} &= U(T) \\
&= e^{-iHT} \\
&= e^{-iE_{00}T}|00\rangle_{ij}\langle 00|_{ij} + e^{-iE_{01}T}|01\rangle_{ij}\langle 01|_{ij} + e^{-iE_{10}T}|10\rangle_{ij}\langle 10|_{ij} + e^{-iE_{11}T}|11\rangle_{ij}\langle 11|_{ij}
\end{aligned}
$$

Comparing the eigenvalues from the spectral decomposition with those from the time evolution operator, the energy eigenvalues can be determined:

$$
\begin{aligned}
e^{-iE_{00}T} &= 1 \implies E_{00} = 0 \\
e^{-iE_{01}T} &= 1 \implies E_{01} = 0 \\
e^{-iE_{10}T} &= 1 \implies E_{10} = 0 \\
e^{-iE_{11}T} &= -1 \implies E_{11} = \frac{\pi}{T}
\end{aligned}
$$

Given these derived eigenvalues, the Hamiltonian that implements the CZ gate on qubits i and j is $H_{\text{operator}} = \pi|11\rangle_{ij}\langle 11|_{ij}$. Notably, using the expression $|11\rangle\langle 11| = \frac{I\otimes I - I\otimes Z - Z\otimes I + Z\otimes Z}{4}$ [48]

demonstrates that the choice of qubits i and j does not influence the resulting Hamiltonian:

$$H_{\text{operator}} = \frac{\pi}{4}(I^{\otimes n} - Z_i - Z_j + Z_i Z_j) \tag{4.32}$$

Here, Z_{ij} denotes the Pauli Z operator acting on the i-th and j-th qubit, with identity operator I on the remaining qubits. In essence, this operator has an eigenvalue of π for the basis states where both qubits i and j are in the $|1\rangle$ state, and an eigenvalue of 0 for all other basis states.

For the control signal, a constant envelope $f(t) = \Omega \approx \pi$ is chosen. There is no carrier-frequency (oscillation), so $\omega_c = 0.0$ and the phase is $\phi_c = 0.0$. Thus, the time-dependent signal $S(t) = \Omega \cos(\omega_c t + \phi_c)$ simplifies to $\Omega \cos(0) = \Omega$. Since the control signal is constant, the rotating frame Hamiltonian is equal to the drive Hamiltonian $H_{rot} = H_{drive}$, as derived in Subsection 4.4.2.

4.7. Numerical Validation

This section details the two key metrics used to evaluate pulse performance against target gates: fidelity and a custom component-wise similarity function. It also highlights the advantages and specific applications of each metric in assessing the accuracy of quantum operations.

Evaluation of the pulse performance against the target gate relies on two significant metrics: fidelity, a standard measure of quantum state overlap, and a custom similarity function. Fidelity directly quantifies the probability of measuring one quantum state in the basis of another, given their respective density matrices, ρ and σ. Mathematically, it is defined as [56]:

$$F(\rho, \sigma) = \left(\text{tr}\sqrt{\sqrt{\rho}\sigma\sqrt{\rho}}\right)^2 \tag{4.33}$$

.

For pure states, this simplifies to the squared overlap (inner product) of the states [56]:

$$F(\rho, \sigma) = F(|\psi\rangle\langle\psi|, |\phi\rangle\langle\phi|) = |\langle\psi_\rho|\psi_\sigma\rangle|^2 \tag{4.34}$$

.

The similarity metric offers a component-wise measure, averaging the similarity of corresponding elements in two pure states. The similarity of each component is determined by the absolute difference between its real and imaginary parts, relative to a defined tolerance threshold.

$$\text{CS}(\langle\psi|, |\phi\rangle) = \frac{1}{N}\sum_{i=1}^{N} cs(\psi_i, \phi_i) \tag{4.35}$$

Let $\Delta_{Re} = |Re(\psi_i) - Re(\phi_i)|$ and $\Delta_{Im} = |Im(\psi_i) - Im(\phi_i)|$. Then, the component similarity $cs(\psi_i, \phi_i)$ is calculated as:

$$cs(\psi_i, \phi_i) = \begin{cases} 1 & \text{if } \Delta_{Re} + \Delta_{Im} \leq \text{tolerance} \\ \max(0, 1 - (\Delta_{Re} + \Delta_{Im})) & \text{otherwise} \end{cases} \tag{4.36}$$

The tolerance used is 1×10^{-6}.

To summarize, fidelity offers several advantages as a metric: it has a physical interpretation, is bounded between 0 and 1, is symmetric, and remains monotonic under quantum operations. In contrast, component-wise similarity is sensitive to global phase. These two metrics are therefore used in conjunction to validate pulse outcomes and understand potential errors. It's important to note that while perfect similarity guarantees perfect fidelity, the converse isn't always true; for instance, if two states differ only by a global phase, making the similarity metric a more stringent measure. For the sake of completeness, it's worth mentioning that while fidelity is the most common metric, other measures like trace distance [8], Hilbert-Schmidt distance, and entanglement measures [87] are also utilized. Fidelity between operators can also be quantified [89, 26].

4.8. Correlation Analysis

This section describes the development of an experimental setup specifically designed to numerically prove Equivalence 1.2. The core of this experiment is a correlation analysis, which begins with the computation of the complex coefficients of the expectation values, and subsequently, defines the correlation analysis for three different quantum circuits.

For a QFM defined by the circuit U as, the output is given by the expectation value $f_U(\boldsymbol{\theta}; x)$ as given by Equation 2.29. This expectation value can be interpreted as the probability of the quantum system being measured in a specific state, which will be the ground state $|g\rangle$ in the following.

Considering a discrete interval $\mathbf{x} = [a, b]$, where $a, b \in \mathbb{R}$ and the parameters $\boldsymbol{\theta}$ are held constant, the FFT algorithm provides an approximation of the complex Fourier coefficients. Let $\{C_k\}_{k=0}^{M-1} := C_0, C_1, \ldots, C_{M-1}$ be the set of significant coefficients:

$$C_k = \frac{1}{b-a} \sum_{x=a}^{b-1} f_{U;\boldsymbol{\theta}}[x] e^{-\frac{i2\pi k}{b-a} p} \tag{4.37}$$

Note that the interval $\mathbf{x}$ is now fixed. Importantly, the resulting set of coefficients $\{\mathrm{C}_k\}$ will vary depending on the specific quantum circuit U and its parameters $\boldsymbol{\theta}$. This relationship can be denoted as:

$$(U, \boldsymbol{\theta}) \rightarrow \{\mathrm{C}_k\} \tag{4.38}$$

This dependency will be the focus of the analysis in the subsequent section.

Three distinct quantum circuits, each consisting of a single layer of the form

$$U(x;\boldsymbol{\theta}) = W(\boldsymbol{\theta})S(x)W(\boldsymbol{\theta}) \tag{4.39}$$

will be defined. The data encoding component $S(x)$ typically a Pauli rotation [119], will be implemented as an $RX(x)$ gate applied to each qubit. The variational ansatz $W(\boldsymbol{\theta})$ will be chosen as C9, an HEC architecture [58] and C15 and from a circuit collection [124]. Note that C15 in this work is a slight deviation from the original circuit, by treating the first gate sequence as part of the repeating ansatz as well, for simplicity the circuit will still be called C15. The inclusion of these three circuits is motivated on the one hand by their entangling capabilities (via CZ and CNOT gates). As elaborated in Section 2.1.3.2, entanglement is a necessary factor for achieving the exponential speedup in quantum computation, making the analysis of such circuits generally more significant. On the other hand by their different complexity in terms of their gate count: C9 has 11 gates, while both the HEC and C15 each possess 16. This results also in a different number of pulses, later described in Section 5.3.

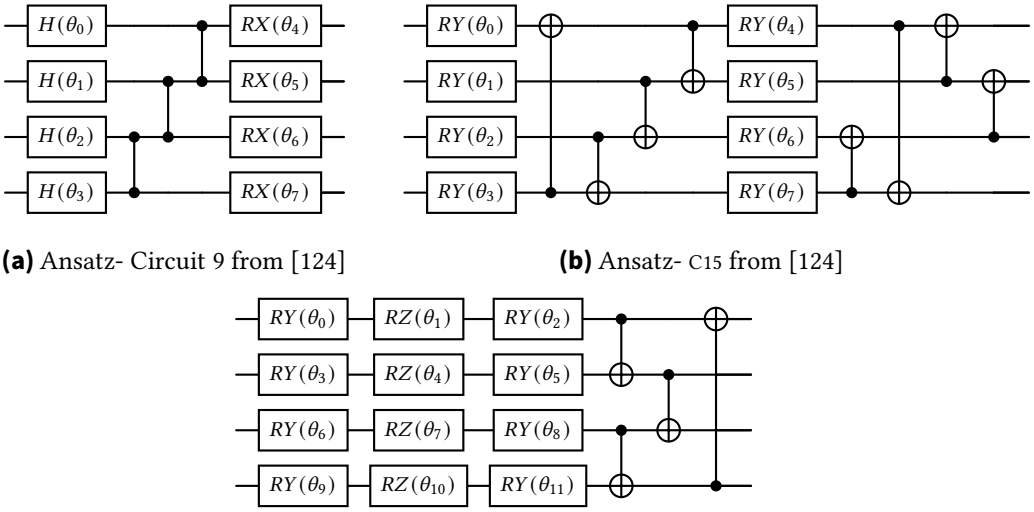

(a) Ansatz- Circuit 9 from [124]

(b) Ansatz- C15 from [124]

(c) Ansatz- HEC from [58]

Figure 4.1.: Circuit diagram of C9, C15 from Ref [124] and the HEC with circular entangling pattern.

For the subsequent analysis, a fixed quantum circuit U is considered. The number of variational parameters, denoted by K, depends on the circuits structure U, such that $\boldsymbol{\theta} \in [-\pi, \pi]^K$. To generate a dataset of circuit outputs, N independent samples of the parameter vector $\boldsymbol{\theta}$ are randomly drawn from $[-\pi, \pi]^K$. This set of parameter samples forms a $N \times K$ matrix $\boldsymbol{\Theta}$:

$$\boldsymbol{\Theta}_{N\times K} = \begin{bmatrix} \boldsymbol{\theta}_1 \\ \boldsymbol{\theta}_2 \\ \vdots \\ \boldsymbol{\theta}_N \end{bmatrix} = \begin{bmatrix} \theta_{1,1} & \theta_{1,2} & \cdots & \theta_{1,K} \\ \theta_{2,1} & \theta_{2,2} & \cdots & \theta_{2,K} \\ \vdots & \vdots & \ddots & \vdots \\ \theta_{N,1} & \theta_{N,2} & \cdots & \theta_{N,K} \end{bmatrix} \tag{4.40}$$

For each of these N parameter variations, the corresponding set of significant complex Fourier coefficients $\{\mathbf{C}_k\}_i$ is calculated. Each coefficient set can be represented as a vector$\boldsymbol{C}_i \in \mathbb{C}^M$, where M is the number of significant complex coefficients. Across all N samples, these coefficient vectors form an $N \times M$ matrix C, where c_{ij} denotes the j-th complex coefficient for the i-th parameter sample.

The analysis will focus on the magnitude of these complex coefficients. The magnitude of the j-th coefficient for the i-th sample is given by $m_{ij} = |c_{ij}| = \sqrt{\mathrm{Re}(c_{ij})^2 + \mathrm{Im}(c_{ij})^2}$ These magnitudes form an $N \times M$ matrix $\mathbf{M}$:

$$\mathbf{M}_{N\times M} = \begin{bmatrix} \mathbf{C}_1 \\ \mathbf{C}_2 \\ \vdots \\ \mathbf{C}_N \end{bmatrix} = \begin{bmatrix} |c_{1,1}| & |c_{1,2}| & \cdots & |c_{1,M}| \\ |c_{2,1}| & |c_{2,2}| & \cdots & |c_{2,M}| \\ \vdots & \vdots & \ddots & \vdots \\ |c_{N,1}| & |c_{N,2}| & \cdots & |c_{N,M}| \end{bmatrix} = \begin{bmatrix} m_{1,1} & m_{1,2} & \cdots & m_{1,M} \\ m_{2,1} & m_{2,2} & \cdots & m_{2,M} \\ \vdots & \vdots & \ddots & \vdots \\ m_{N,1} & m_{N,2} & \cdots & m_{N,M} \end{bmatrix} \tag{4.41}$$

A correlation matrix $\mathbf{R}_{K\times M}$ will be computed, where the element R_{kj} represents the Pearson correlation coefficient between the k-th parameter across all N samples, and the magnitude of the j-th coefficient as well across all N samples.

The Pearson correlation coefficient [136] between two random variables X and Y is defined as:

$$\rho_{X,Y} = \frac{\mathrm{cov}(X, Y)}{\sigma_X \sigma_Y} \tag{4.42}$$

where: where $\mathrm{cov}(X, Y)$ is the covariance of X and Y, and σ_X and σ_Y are the standard deviations of X and Y, respectively.

In this context, X represents the k-th parameter across all N samples, which can be extracted as the k-th column of the parameter matrix Θ:

$$\boldsymbol{\Theta} = \begin{bmatrix} \theta_{1,1} & \theta_{1,2} & \cdots & \boldsymbol{\theta_{1,k}} & \cdots & \theta_{1,K} \\ \theta_{2,1} & \theta_{2,2} & \cdots & \boldsymbol{\theta_{2,k}} & \cdots & \theta_{2,K} \\ \vdots & \vdots & \ddots & \vdots & \ddots & \vdots \\ \theta_{N,1} & \theta_{N,2} & \cdots & \boldsymbol{\theta_{N,k}} & \cdots & \theta_{N,K} \end{bmatrix} \tag{4.43}$$

So, $\boldsymbol{\theta}^{(k)}$ is defined as:

$$\boldsymbol{\theta}^{(k)} = \begin{bmatrix} \theta_{1,k} \\ \theta_{2,k} \\ \vdots \\ \theta_{N,k} \end{bmatrix} \tag{4.44}$$

And Y represents the magnitudes of the j-th complex coefficient across all N samples, which can be extracted as the j-th column of the magnitude matrix $\mathbf{M}$:

$$\mathbf{M} = \begin{bmatrix} m_{1,1} & m_{1,2} & \cdots & \mathbf{m_{1,j}} & \cdots & m_{1,M} \\ m_{2,1} & m_{2,2} & \cdots & \mathbf{m_{2,j}} & \cdots & m_{2,M} \\ \vdots & \vdots & \ddots & \vdots & \ddots & \vdots \\ m_{N,1} & m_{N,2} & \cdots & \mathbf{m_{N,j}} & \cdots & m_{N,M} \end{bmatrix} \tag{4.45}$$

Therefore, $\mathbf{m}^{(j)}$ is:

$$\mathbf{m}^{(j)} = \begin{bmatrix} m_{1,j} \\ m_{2,j} \\ \vdots \\ m_{N,j} \end{bmatrix} \tag{4.46}$$

Finally, the Pearson correlation coefficient R_{kj}, is defined as:

$$R_{kj} = \frac{\sum_{i=1}^{N}(\theta_{1,k} - \bar{\boldsymbol{\theta}}^{(k)})(m_{ij} - \bar{\mathbf{m}}_j)}{\sqrt{\sum_{i=1}^{N}(\theta_{1,k} - \bar{\boldsymbol{\theta}}^{(k)})^2 \sum_{i=1}^{N}(m_{ij} - \bar{\mathbf{m}}_j)^2}} \tag{4.47}$$

Here, $\bar{\boldsymbol{\theta}}^{(k)} = \frac{1}{N}\sum_{i=1}^{N}\theta_{1,k}$ represents the mean of the k-th parameter across all N samples, and $\bar{\mathbf{m}}_j = \frac{1}{N}\sum_{i=1}^{N} m_{ij}$ is the mean of the magnitudes of the j-th coefficient across all N samples.

5. Results

This chapter presents the findings and results of this work. Section 5.1 provides an overview of the numerical simulation frameworks in the field of quantum dynamics. Section 5.2 offers insights into this work's pulse-level framework $f'_{\theta,\Pi}$. First, the modulated control signal used to achieve a qubit's state transition is illustrated. Next, pseudocode is shown to demonstrate the algorithmic process of applying a pulse-level gate. The visual effect of the pulse on the qubit's state is shown in Table A.3. The main validation work, which numerically proves the pulse-level framework, is presented in Section 5.3.

5.1. Simulation Frameworks

Abstract gate-based quantum computing has various computational frameworks with unique advantages [125]. For simulation of quantum dynamics, Qiskit Pulse [3] (deprecated and migrated to Qiskit Dynamics [101]) and QuTiP [55] are two prominent frameworks [82].

QuTiP is a well-established open-source Python package. It contains the Qutip-qip module, which focuses on pulse-level quantum information processing with key features including comprehensive open quantum system tools, strong noise modeling, predefined hardware models, and optimal control [55].

Qiskit Dynamics on the other hand benefits from highly configurable settings, offering users the choice of computational backends like NumPy/SciPy for general scientific computing or JAX, which provides automatic differentiation, GPU acceleration, and compilation for enhanced performance. Additionally, it allows selection of dense or sparse data representations to optimize memory and speed, various solvers (standard ODE or exponentiation), and automated model transformations (rotating frames, rotating wave approximation as detailed in Subsection 2.1.1) [96]. It benefits from active development and strong Qiskit community support as well. Benchmarking shows Qiskit Dynamics significantly faster than QuTiP, e.g. for gate parameter tuning for a 3-qubit system [97] while also having the advantage of being differentiable [97].

There are other simulation frameworks allowing for simulating quantum systems like SimuQ [90] which is specifically designed for analog quantum simulation, supporting Hamiltonian programming and targeting diverse analog hardware (superconducting, neutral-atom, trapped-ion and even d-wave) or Amazon Braket which supports analog Hamiltonian simulation on specific hardware, enabling direct programming of the system Hamiltonian [144].

An extensive comparison of the language as well as target hardware between different simulation frameworks can be found in Table A.2. Due to its superior speed, its differentiability and flexibility in simulating Quantum systems, Qiskit Dynamics is utilized for the simulation of this work.

5.2. Numerical Implementation

This section details the numerical approach used to simulate quantum circuits at the pulse-level, illustrated for the fundamental X-rotation pulse on a single qubit. This section first illustrates the numerical implementation before delving into the details of the control signals.

The implementation for the pulse-level framework and the code to reproduce all plots, such as those presented in Figure 5.2 and Table A.3, are accessible on GitHub [113]. The core logic for pulse simulation is found within the *PulseBackend* class. A simple pseudocode to demonstrate the algorithmic process of applying a X-rotation in the *PulseBackend* class is illustrated in Figure 5.1.

```
CLASS PulseBackend:

    PROPERTIES:
        number_qubits
        current_state
        pulse_operator // Manages pulse operations like constructing Hamiltonians

    METHOD apply_rx_pulse(rotation_angle, target_qubits):

        CALCULATE the required pulse parameters based on the rotation angle

        DEFINES the control signal, static and drive Hamiltonian and rotation frame

        SOLVE / SIMULATE the Schrödinger equation

        UPDATE the current_state with the final state after the evolution
```

Figure 5.1.: Pseudocode of the *PulseBackend* class.

In the following, it is shown how the needed pulse for the X-rotation is constructed with the needed parameters A, σ, ν and ϕ_c, as defined in Subsection 4.4.1. The time interval used for illustration is adapted for better visualizing each signal, e.g. a broader interval is used for the Gaussian envelope to show its full decay, while a narrower interval is used for the oscillating term to highlight its periodic nature. The Gaussian envelope is defined to modulate the carrier frequency, which is set to the qubit's transition frequency. Figure 5.2a illustrates the temporal shape of this Gaussian envelope, spanning from 0 to 60 nanoseconds,

with control parameters, $A = 1.0$ and standard deviation $\sigma = 15$. The carrier frequency, $\nu = \frac{\omega}{2\pi} = \frac{10\pi}{2\pi} = 5\,\text{GHz}$, combined with a phase $\phi_c = 0.0$ defines an oscillating cosine term (5 periods per nanosecond). This oscillating term is visualized within the 11.5 to 12.5 ns time interval in Figure 5.2b. The combination of these components results in the modulated control signal shown in Figure 5.2c, active from 10 to 25 nanoseconds.

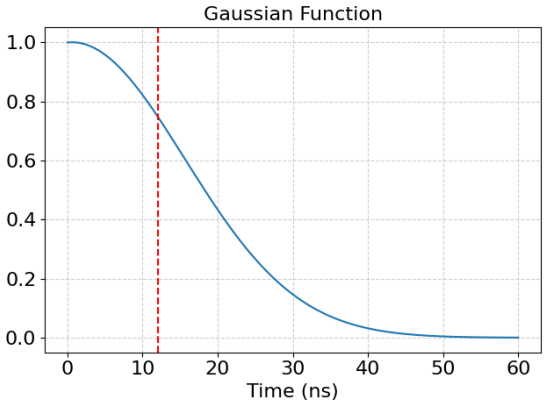

(a) Gaussian function

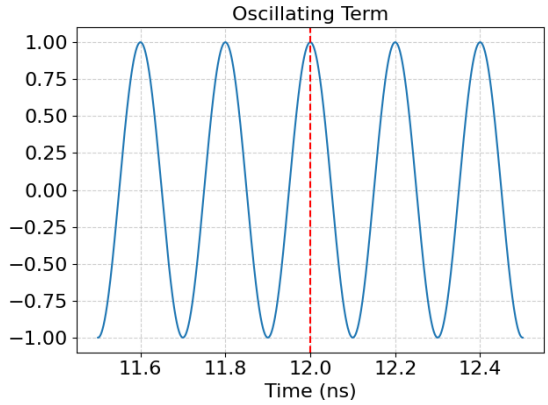

(b) Oscillating term

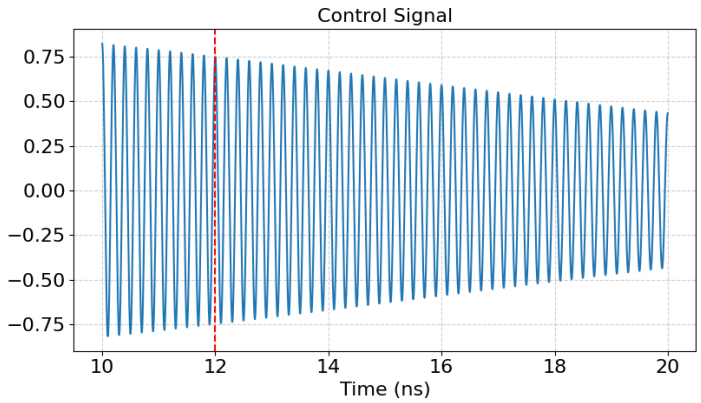

(c) The resulting control signal

Figure 5.2.: The gaussian function (a) modulated by the oscillating term (b) results in the control signal (c).

5.3. Validation Experiments

This section presents the main results of the work based on the experiment setup described in Section 4.8. The numerical evaluation focused on the three circuits with entangling capabilities: C9, the HEC, and C15. These circuits are selected to assess the scalability of the framework due to their distinct pulse requirements detailed in Table 5.1. This variability in pulse counts stems from the pulse description of the distinct quantum gates derived in Chapter 4; single pulses for Rotation and CZ gates (Subsections 4.4.1 and 4.4.2), three pulses

for Hadamard gates (Subsection 4.4.3 and 4.6) and seven pulses for CNOT gates (Subsection 4.6). The parameters for pulse-level evaluation are initially set based on theoretical estimations and refined through manual tuning.

To ensure a robust evaluation, 5000 randomly sampled parameter sets are generated for evaluation, consistent with the methodology in Sim et al. [124]. Both the implemented pulse simulation backend [113] and the gate-level simulation using the PennyLane framework [131] are utilized to simulate these quantum circuits.

As described in Section 4.8, the parameter-magnitude correlation matrix is computed for each circuit, comparing both the gate-level and pulse-level evaluations. The results of this correlation are depicted in Table 5.2 for C9, HEC and the C15 respectively. Here, the left-hand column depicts the correlation result for the pulse-based evaluation while the plots in the right-hand column visualize the difference to the gate-based evaluation. The MAE of these correlations are summarized in Table 5.1. For additional context, the MAE of the coefficient magnitudes (the direct output after DFT before the correlation with the parameter values) is provided as well. The experimental results consistently demonstrate a relatively small deviation between the gate-level and pulse-level QFM evaluations, with the MAE consistently in the order of 10^{-4} to 10^{-5}.

	C9	HEC	C15
Number of pulses	24	84	132
MAE before correlation	0.000159	0.000289	0.000111
MAE after correlation	0.000369	0.000197	0.000069

Table 5.1.: Number of pulses, as well as the MAE before and after the correlation with the parameters for each circuit.

The evaluations are performed using the CPUs on the *bwUniCluster 3.0* [129], specifically leveraging 64 CPUs for parallel processing of samples when simulating more complex circuits such as HEC and C15.

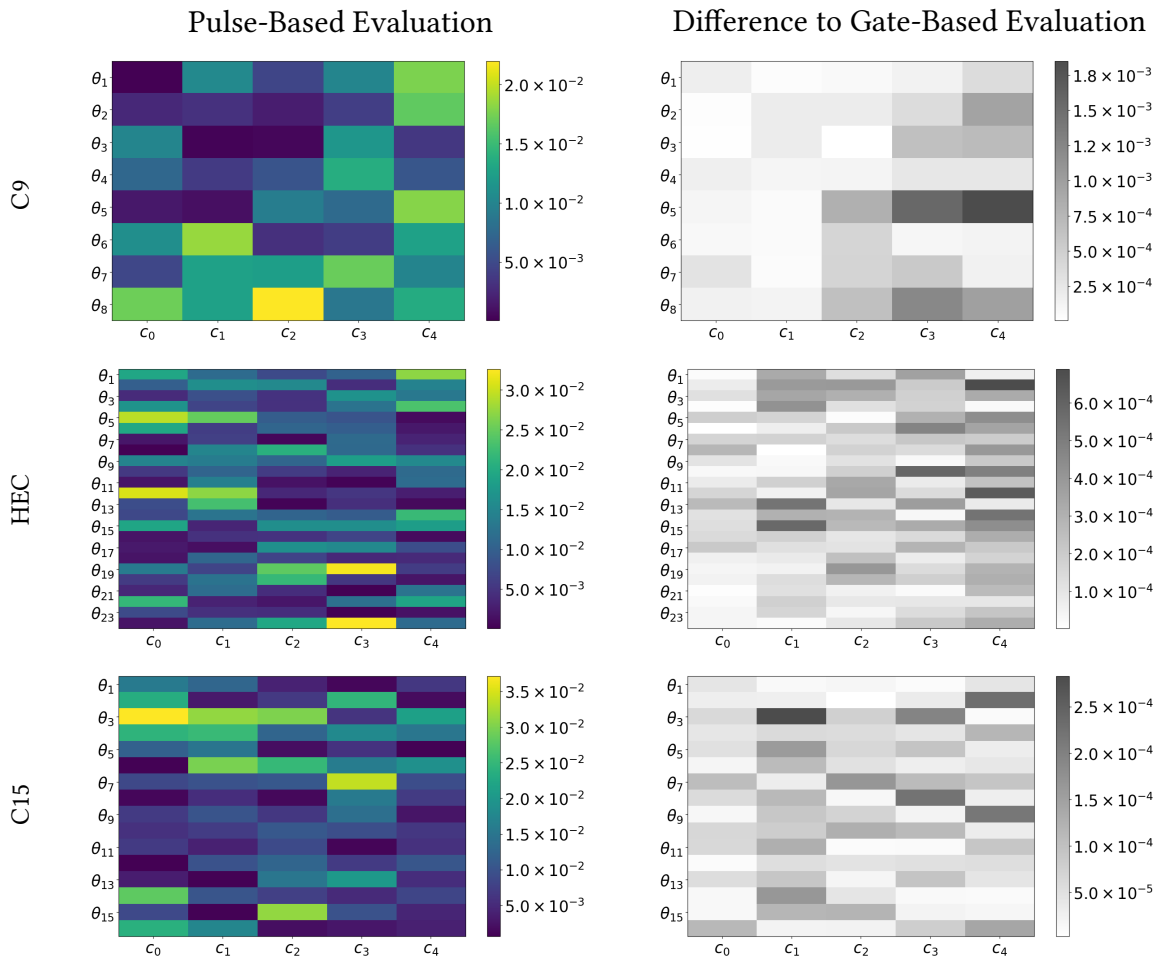

Table 5.2.: Correlation matrices for pulse-based evaluation and difference to the gate-based evaluation for each circuit.

6. Discussion

The decision to adopt Qiskit Dynamics as the primary framework for modeling at the pulse-level proved to be a successful choice. Its high degree of configurability enables precise representations of the intricate quantum dynamics and allows capturing the subtle operations happening at the hardware level. Furthermore, the inherent differentiability of Qiskit Dynamics [97] offers a significant advantage, paving the way for applying classical optimization techniques, which will be discussed in the context of future work in Chapter 7.

The numerical implementation of the pulse-level models directly reflects the physical control mechanisms employed in leading quantum computing architectures. Specifically, the approach involved modeling control pulses using Gaussian or constant envelopes combined with oscillating terms to represent the applied electromagnetic signals. This methodology, which involved solving the quantum dynamics for both static and time-dependent (drive) Hamiltonians, closely aligns with the operational principles of superconducting qubit and trapped ion quantum hardware, as detailed in Section 2.2.1. Consequently, the framework is generally applicable to these two prominent quantum platforms.

Notably, the demanding nature of pulse-level simulations, which involved solving the dynamics multiple times for one gate, necessitated significant computational resources and made parallel processing necessary for evaluation.

The low MAE provides strong evidence for the theoretical equivalence established in Chapter 1 and confirms the feasibility of representing gate-level QFM at the pulse-level:

$$f_{\theta}(x) = \sum_{\omega \in \Omega} c_{\omega}(\theta) e^{ix\omega} \equiv \sum_{\omega \in \Omega} c_{\omega}(\theta, \Pi) e^{ix\omega} =: f'_{\theta,\Pi}(x) \tag{6.1}$$

As described in Section 5.3, the pulse parameters are initially set based on theoretical estimations and refined through manual tuning. We anticipate that carrying out classical optimization techniques would significantly enhance the accuracy and fidelity of the pulse-level representation, potentially leading to even lower MAE values and higher effective gate fidelity.

The deviations of the MAE values between the different circuits could indicate that some pulse-level gates are more responsible for deviations and therefore contribute disproportionately to the observed error.

An intriguing observation was the counterintuitive trend of decreasing MAE for the correlation values with increased model complexity, i.e., with increasing number of pulses. One

might initially hypothesize that an increase in the number of free parameters and pulse components would lead to increased error accumulation. However, the results suggest that the additional degrees of freedom provided by more pulses enabled a more precise approximation of the target gate-level operations, or at least that increasing model complexity did not lead to an accumulation of errors.

While an intriguing decrease in MAE was observed with increased model complexity it is also important to acknowledge that this trend might be influenced by the use of different circuits. Specifically, lighter circuits potentially used for higher pulse counts could contribute to the reduced error. Thus, even with lower apparent MAE, we cannot definitively rule out error accumulation.

7. Conclusion and Outlook

This work establishes a theoretical and numerical framework $f'_{\theta,\Pi}$ for evaluating QFMs at the pulse-level, demonstrating a high degree of equivalence with the gate-level evaluation. By leveraging Qiskit Dynamics, numerical validation showed that complex quantum circuits can be accurately represented and simulated through precisely shaped electromagnetic pulses, extending the applicability of QFMs to a deeper, lower-level layer of quantum control.

While the framework proved robust, there are areas for refinement. The current pulse parameters are initialized based on theoretical estimations and then manually tuned. A more sophisticated approach involves classical optimization techniques, which would probably lead to even higher gate fidelity and further reduce the observed deviations as already implied in Chapter 6. This would not only improve the accuracy of the pulse-level QFMs but also streamline the parameter tuning process.

A clear next step would be to **expand experimental validation** to a more extensive collection of circuits, particularly those from the Sim et al. [124] benchmark. This would help verify if increased model complexity (i.e., more pulses) truly doesn't influence deviation or accumulate errors.

The framework itself offers a great possibility for further research as well. Due to the finer control on pulse-level two major areas can be explored in this context. One promising direction is **error analysis and mitigation**. The framework could be utilized to simulate and analyze the influence of control errors in quantum hardware. For instance, experiments could be re-conducted with slightly varied pulse parameters to observe patterns in deviations from ideal gate evaluations. This would enhance our understanding of such errors, which could, in turn, support the development of more effective error mitigation strategies.

Another exciting avenue lies in **expressivity analysis and enhancement**. As discussed, the differentiability of the implemented framework enables the direct training of pulse parameters using classical optimization techniques. This capability opens the door to exploring whether metrics often analyzed in the context of QFMs, such as expressiveness or entangling capabilities, could be further analyzed and possibly enhanced. One could investigate which pulse parameters significantly impact these metrics and then train them with classical optimization techniques to achieve improvements. Relevant literature for pulse control optimization in this area includes sampling-based learning methods for generating universal quantum gates [34], gradient-type algorithms [93], and reinforcement learning approaches [13].

Beyond immediate extensions, further research could focus on rethinking and evolving the framework itself:

- **Broader Hardware Applicability:** Investigating the direct applicability of this framework to other real-world quantum hardware implementations beyond superconducting qubits and trapped-ions, especially those with fundamentally different control mechanisms. This would expand the understanding of the constraints and opportunities presented by different physical implementations.
- **Modeling Noise with Density Matrices:** To enable more realistic simulations, the framework could be extended to model noise by incorporating density matrices for mixed states, as described in Section 2.1.2.1. This extension is feasible with Qiskit Dynamics, which supports solving Lindblad dynamics [25] and would allow to provide and analyze on a more realistic simulation framework.
- **Optimizing Hamiltonian Complexity:** An intriguing avenue involves exploring whether complex circuits can be implemented with only one or very few Hamiltonians of higher complexity. This could potentially achieve the desired circuit manipulation with less computational expense during runtime. Analyzing the custom Hamiltonian dynamics in terms of **error analysis and mitigation** and **expressivity analysis and enhancement**, as discussed before, would provide a deeper understanding of hardware-level optimization.

Ultimately, these future research avenues aim to bridge the gap between theoretical models and practical quantum hardware, analyzing further the underlying physics of quantum operations.

Bibliography

[1] John R. Albright. "Effect of Electric and Magnetic Fields On Quantum Systems". In: (2022). https://www.ebsco.com/research-starters/physics/effect-electric-and-magnetic-fields-quantum-systems.

[2] Thomas Alexander et al. "Qiskit pulse: programming quantum computers through the cloud with pulses". In: *Quantum Science and Technology* 5.4 (2020). Published 18 August 2020, p. 044006. DOI: 10.1088/2058-9565/aba404.

[3] Thomas Alexander et al. "Qiskit pulse: programming quantum computers through the cloud with pulses". In: *Quantum Science and Technology* 5.4 (Aug. 2020), p. 044006. ISSN: 2058-9565. DOI: 10.1088/2058-9565/aba404. URL: http://dx.doi.org/10.1088/2058-9565/aba404.

[4] Herbert Amann et al., eds. *Functional Analysis and Evolution Equations: The Günter Lumer Volume*. Basel: Birkhäuser, 2008. ISBN: 978-3-7643-7793-9. DOI: 10.1007/978-3-7643-7794-6.

[5] Jeeva Anandan and Jun Suzuki. "Quantum Mechanics in a Rotating Frame". In: *Relativity in Rotating Frames: Relativistic Physics in Rotating Reference Frames*. Ed. by Guido Rizzi and Matteo Luca Ruggiero. Dordrecht: Springer Netherlands, 2004, pp. 361–370. ISBN: 978-94-017-0528-8. DOI: 10.1007/978-94-017-0528-8_19. URL: https://doi.org/10.1007/978-94-017-0528-8_19.

[6] Q Ansel et al. "Introduction to theoretical and experimental aspects of quantum optimal control". In: *Journal of Physics B: Atomic, Molecular and Optical Physics* 57.13 (June 2024), p. 133001. ISSN: 1361-6455. DOI: 10.1088/1361-6455/ad46a5. URL: http://dx.doi.org/10.1088/1361-6455/ad46a5.

[7] Alvaro Ballon. *Quantum machine learning with trapped ions*. Accessed: April 30, 2025. URL: https://pennylane.ai/qml/demos/tutorial_trapped_ions.

[8] S. M. Barnett. "Quantum Information". In: Oxford University Press, 2009. Chap. 4.

[9] Gerard G. A. Bäuerle and Eddy A. de Kerf. *Lie Algebras, Part 1: Finite and Infinite Dimensional Lie Algebras and Applications in Physics*. Studies in Mathematical Physics. Amsterdam: North Holland, 1990. ISBN: 0-444-88776-8.

[10] Ville Bergholm et al. *PennyLane: Automatic differentiation of hybrid quantum-classical computations*. 2022. arXiv: 1811.04968 [quant-ph]. URL: https://arxiv.org/abs/1811.04968.

[11] Rajendra Bhatia. *Matrix Analysis*. Vol. 169. Graduate Texts in Mathematics. Springer, 1997. ISBN: 978-0-387-94846-1.

[12] Paul E. Black, D. Richard Kuhn, and Carl J. Williams. "Quantum Computing and Communication". In: ed. by Marvin V. Zelkowitz. Vol. 56. Advances in Computers. Elsevier, 2002, pp. 189–244. DOI: https://doi.org/10.1016/S0065-2458(02)80007-9. URL: https://www.sciencedirect.com/science/article/pii/S0065245802800079.

[13] Adrien Bolens and Markus Heyl. "Reinforcement Learning for Digital Quantum Simulation". In: *Phys. Rev. Lett.* 127 (11 Sept. 2021), p. 110502. DOI: 10.1103/PhysRevLett.127.110502. URL: https://link.aps.org/doi/10.1103/PhysRevLett.127.110502.

[14] Stefano Bosco et al. "Phase-Driving Hole Spin Qubits". In: *Phys. Rev. Lett.* 131 (19 Nov. 2023), p. 197001. DOI: 10.1103/PhysRevLett.131.197001. URL: https://link.aps.org/doi/10.1103/PhysRevLett.131.197001.

[15] Sébastien Bourdeauducq et al. *Artiq 1.0*. 2016.

[16] Elbert Oran Brigham. *The fast Fourier transform*. Nachdr. Englewood Cliffs, N.J: Prentice-Hall, 1974. ISBN: 978-0-13-307496-3.

[17] Cahyati. *Rabi Drive and Ramsey Experiment*. Accessed May 3, 2025. 2020. URL: https://cahyati2d.medium.com/rabi-drive-ramsey-experiment-c14ff626e719.

[18] Tommaso Caneva, Tommaso Calarco, and Simone Montangero. "Chopped random-basis quantum optimization". In: *Physical Review A* 84.2 (Aug. 2011). ISSN: 1094-1622. DOI: 10.1103/physreva.84.022326. URL: http://dx.doi.org/10.1103/PhysRevA.84.022326.

[19] Marco Cerezo et al. "Variational quantum algorithms". In: *Nature Reviews Physics* 3.9 (2021), pp. 625–644.

[20] Jwo-Sy Chen et al. "Benchmarking a trapped-ion quantum computer with 30 qubits". In: *Quantum* 8 (2024). Published: 2024-11-07, p. 1516. DOI: 10.22331/q-2024-11-07-1516. eprint: 2308.05071v2.

[21] E. Chertkov, J. Bohnet, D. Francois, et al. "Holographic dynamics simulations with a trapped-ion quantum computer". In: *Nature Physics* 18 (2022), pp. 1074–1079. DOI: https://doi.org/10.1038/s41567-022-01689-7.

[22] J. Ignacio Cirac et al. *Quantum algorithms for quantum simulation*. 2024. arXiv: 2402.12356 [quant-ph].

[23] Qiskit Community. *qiskit_dynamics/signals/signals.py*. Accessed May 4, 2025. 2025. URL: https://github.com/qiskit-community/qiskit-dynamics/blob/main/qiskit_dynamics/signals/signals.py.

[24] Qiskit Dynamics Community. *How to Configure Simulations*. Accessed May 3, 2025. URL: https://qiskit-community.github.io/qiskit-dynamics/userguide/how_to_configure_simulations.html.

[25] Qiskit Dynamics Community. *Lindblad Dynamics Simulation*. Accessed 2025-05-01. URL: https://qiskit-community.github.io/qiskit-dynamics/tutorials/Lindblad_dynamics_simulation.html.

[26] Qiskit Dynamics Community. *Optimizing Pulse Sequence*. Accessed May 3, 2025. URL: https://qiskit-community.github.io/qiskit-dynamics/tutorials/optimizing_pulse_sequence.html.

[27] Rigetti Computing. *Quil Language Specification*. Accessed 2025-05-02. URL: https://pyquil-docs.rigetti.com/en/stable/quilt.html.

[28] Jay Theodore Cremer. "14 - The Klein–Gordon and Dirac Equations". In: *Neutron and X-ray Optics*. Ed. by Jay Theodore Cremer. Oxford: Elsevier, 2013, pp. 813–888. ISBN: 978-0-12-407164-3. DOI: https://doi.org/10.1016/B978-0-12-407164-3.00013-9. URL: https://www.sciencedirect.com/science/article/pii/B9780124071643000139.

[29] Aniket S. Dalvi et al. "Graph-Based Pulse Representation for Diverse Quantum Control Hardware". In: (2024). arXiv: 2409.08407 [quant-ph].

[30] Aniket S. Dalvi et al. *Graph-Based Pulse Representation for Diverse Quantum Control Hardware*. 2024. arXiv: 2409.08407 [quant-ph]. URL: https://arxiv.org/abs/2409.08407.

[31] J. C. Diels and E. L. Hahn. "Carrier-Frequency Distance Dependence of a Pulse Propagating in a Two-Level System". In: *Phys. Rev. A* 8 (2 Aug. 1973), pp. 1084–1110. DOI: 10.1103/PhysRevA.8.1084. URL: https://link.aps.org/doi/10.1103/PhysRevA.8.1084.

[32] P. A. M. Dirac. "A new notation for quantum mechanics". In: *Mathematical Proceedings of the Cambridge Philosophical Society* 35.3 (1939). Also see his standard text, The Principles of Quantum Mechanics, IV edition, Clarendon Press (1958), ISBN 978-0198520115, pp. 416–418. DOI: 10.1017/S0305004100021162.

[33] P. A. M. Dirac. "Relativistic Wave Equations". In: *Proceedings of the Royal Society of London. Series A, Containing Papers of a Mathematical and Physical Character* 155.881 (1936), pp. 447–459. DOI: 10.1007/BF01011696.

[34] D. Dong et al. "Learning robust pulses for generating universal quantum gates". In: *Scientific Reports* 6 (2016), p. 36090.

[35] Daoyi Dong et al. "Learning robust pulses for generating universal quantum gates". In: *Scientific Reports* 6.1 (2016), p. 36090. DOI: 10.1038/srep36090.

[36] Ian Duck and E.C.G. Sudarshan. "Dirac's Invention of Quantum Field Theory". In: *Pauli and the Spin-Statistics Theorem*. World Scientific Publishing, 1998. Chap. 6, pp. 149–167. ISBN: 978-9810231149.

[37] F. J. Dyson. "The Radiation Theories of Tomonaga, Schwinger, and Feynman". In: *Phys. Rev.* 75 (3 Feb. 1949), pp. 486–502. DOI: 10.1103/PhysRev.75.486. URL: https://link.aps.org/doi/10.1103/PhysRev.75.486.

[38] Albert Einstein, Boris Podolsky, and Nathan Rosen. "Can Quantum-Mechanical Description of Physical Reality Be Considered Complete?" In: *Physical Review* 47.10 (1935), pp. 777–780. DOI: 10.1103/PhysRev.47.777.

[39] Richard Fitzpatrick. *5.2: Non-interacting Particles*. Accessed May 1, 2025. URL: https://phys.libretexts.org/Bookshelves/Quantum_Mechanics/Introductory_Quantum_Mechanics_(Fitzpatrick)/05%3A_Multi-Particle_Systems/5.02%3A_Non-interacting_Particles.

[40] Enrico Fontana et al. *Classical simulations of noisy variational quantum circuits*. 2023. arXiv: 2306.05400 [quant-ph]. URL: https://arxiv.org/abs/2306.05400.

[41] Enrico Fontana et al. *Spectral analysis for noise diagnostics and filter-based digital error mitigation*. 2022. arXiv: 2206.08811 [quant-ph]. URL: https://arxiv.org/abs/2206.08811.

[42] Christopher Foot. *Atomic Physics*. New York: Oxford University Press, 2005.

[43] P. de Fouquieres et al. "Second order gradient ascent pulse engineering". In: *Journal of Magnetic Resonance* 212.2 (Oct. 2011), pp. 412–417. ISSN: 1090-7807. DOI: 10.1016/j.jmr.2011.07.023. URL: http://dx.doi.org/10.1016/j.jmr.2011.07.023.

[44] Michael Fowler. *3.9: Appendix: Some Exponential Operator Algebra*. Accessed May 2, 2025. URL: https://phys.libretexts.org/Bookshelves/Quantum_Mechanics/Quantum_Mechanics_(Fowler)/03%3A_Mostly_1-D_Quantum_Mechanics/3.09%3A_Appendix-_Some_Exponential_Operator_Algebra.

[45] Raytheon BBN Technologies Quantum Group. *QGL*. 2020. URL: https://github.com/BBN-Q/QGL.

[46] Roger A. Horn and Charles R. Johnson. *Topics in Matrix Analysis*. Cambridge University Press, 1991. ISBN: 978-0-521-46713-1.

[47] Ryszard Horodecki et al. "Quantum entanglement". In: *Nature Physics* 3.8 (July 2007), pp. 523–529. DOI: https://doi.org/10.48550/arXiv.quant-ph/0702225. URL: https://arxiv.org/abs/quant-ph/0702225.

[48] Sebastian Horvat, Xiaoqin Gao, and Borivoje Dakić. "Universal quantum computation via quantum controlled classical operations". In: *Journal of Physics A: Mathematical and Theoretical* 55 (Jan. 2022). DOI: 10.1088/1751-8121/ac4393.

[49] Simon Humpohl et al. *qutech/qupulse: qupulse 0.10*. 2024.

[50] Eric Hyyppä et al. "Reducing Leakage of Single-Qubit Gates for Superconducting Quantum Processors Using Analytical Control Pulse Envelopes". In: *PRX Quantum* 5.3 (Sept. 2024). ISSN: 2691-3399. DOI: 10.1103/prxquantum.5.030353. URL: http://dx.doi.org/10.1103/PRXQuantum.5.030353.

[51] Mohannad Ibrahim et al. *Pulse-Level Optimization of Parameterized Quantum Circuits for Variational Quantum Algorithms*. Nov. 2022. DOI: 10.48550/arXiv.2211.00350.

[52] Zurich Instruments. *zurich-instruments/laboneq: Labone q 2.39.0*. URL: https://www.zhinst.com/europe/en/quantum-computing-systems/labone-q.

[53] Josh Izaac. *Endian-ness of circuit simulator*. July 8, 2021. URL: https://discuss.pennylane.ai/t/endian-ness-of-circuit-simulator/1797/3 (visited on 04/30/2025).

[54] Ben Jaderberg et al. "Let quantum neural networks choose their own frequencies". In: *Physical Review A* 109.4 (Apr. 2024). ISSN: 2469-9934. DOI: 10.1103/physreva.109.042421. URL: http://dx.doi.org/10.1103/PhysRevA.109.042421.

[55] J.R. Johansson, P.D. Nation, and Franco Nori. "QuTiP: An open-source Python framework for the dynamics of open quantum systems". In: *Computer Physics Communications* 183.8 (2012), pp. 1760–1772. ISSN: 0010-4655. DOI: https://doi.org/10.1016/j.cpc.2012.02.021. URL: https://www.sciencedirect.com/science/article/pii/S0010465512000835.

[56] Richard Jozsa. "Fidelity for Mixed Quantum States". In: *Journal of Modern Optics* 41.12 (1994), pp. 2315–2323. DOI: 10.1080/09500349414552171.

[57] Richard Jozsa and Noah Linden. "On the role of entanglement in quantum-computational speed-up". In: *Proceedings of the Royal Society of London. Series A: Mathematical, Physical and Engineering Sciences* 459.2036 (Aug. 2003), pp. 2011–2032. ISSN: 1471-2946. DOI: 10.1098/rspa.2002.1097. URL: http://dx.doi.org/10.1098/rspa.2002.1097.

[58] Abhinav Kandala et al. "Hardware-efficient variational quantum eigensolver for small molecules and quantum magnets". In: *Nature* 549.7671 (Sept. 2017), pp. 242–246. ISSN: 1476-4687. DOI: 10.1038/nature23879. URL: http://dx.doi.org/10.1038/nature23879.

[59] Jeongsoo Kang and Younghun Kwon. *Construction of new type of CNOT gate using cross-resonance pulse in the transmon-PPQ system*. 2025. arXiv: 2501.15218 [quant-ph]. URL: https://arxiv.org/abs/2501.15218.

[60] Muhammad Qasim Khan et al. "SPAM-robust multi-axis quantum noise spectroscopy in temporally correlated environments". In: *arXiv preprint arXiv:2402.12361* (2024).

[61] Youngseok Kim et al. "Scalable error mitigation for noisy quantum circuits produces competitive expectation values". In: *Nature Physics* 19.5 (Feb. 2023), pp. 752–759. ISSN: 1745-2481. DOI: 10.1038/s41567-022-01914-3. URL: http://dx.doi.org/10.1038/s41567-022-01914-3.

[62] A Yu Kitaev. "Quantum computations: algorithms and error correction". In: *Russian Mathematical Surveys* 52.6 (Dec. 1997), pp. 1191–1249. ISSN: 0036-0279. DOI: 10.1070/rm1997v052n06abeh002155.

[63] Océane Koska, Marc Baboulin, and Arnaud Gazda. *A tree-approach Pauli decomposition algorithm with application to quantum computing*. 2024. arXiv: 2403.11644 [quant-ph]. URL: https://arxiv.org/abs/2403.11644.

[64] P. Krantz et al. "A quantum engineer's guide to superconducting qubits". In: *Applied Physics Reviews* 6.2 (June 2019), p. 021318. ISSN: 1931-9401. DOI: 10.1063/1.5089550. eprint: https://pubs.aip.org/aip/apr/article-pdf/doi/10.1063/1.5089550/16667201/021318_1_online.pdf. URL: https://doi.org/10.1063/1.5089550.

[65] Jonas Landman et al. *Classically Approximating Variational Quantum Machine Learning with Random Fourier Features*. 2022. arXiv: 2210.13200 [quant-ph]. URL: https://arxiv.org/abs/2210.13200.

[66] Jonathan Wei Zhong Lau et al. "NISQ computing: where are we and where do we go?" In: *AAPPS bulletin* 32.1 (2022), p. 27.

[67] Lewoody. *Quantum Endianness*. Dec. 16, 2021. URL: https://lewoody.com/2021/12/16/quantum-endianess/ (visited on 04/30/2025).

[68] B. Li, T. Calarco, and F. Motzoi. "Experimental error suppression in Cross-Resonance gates via multi-derivative pulse shaping". In: *npj Quantum Information* 10.1 (2024), p. 66. DOI: 10.1038/s41534-024-00863-4. URL: https://doi.org/10.1038/s41534-024-00863-4.

[69] Boxi Li et al. "Pulse-level noisy quantum circuits with QuTiP". In: *Quantum* 6 (Jan. 2022), p. 630. ISSN: 2521-327X. DOI: 10.22331/q-2022-01-24-630. URL: http://dx.doi.org/10.22331/q-2022-01-24-630.

[70] Zhiding Liang et al. *NAPA: Intermediate-level Variational Native-pulse Ansatz for Variational Quantum Algorithms*. 2024. arXiv: 2208.01215 [quant-ph]. URL: https://arxiv.org/abs/2208.01215.

[71] Chyi-Lung Lin. *Analyzing the Time Evolution of Wave Functions by Decomposing the Hamiltonian into State-Preserving and State-Changing Hamiltonians*. 2014. arXiv: 1407.3438 [quant-ph]. URL: https://arxiv.org/abs/1407.3438.

[72] N. M. Linke et al. "Experimental comparison of two quantum computing architectures". In: *Proceedings of the National Academy of Sciences of the United States of America* 114.13 (2017), pp. 3305–3310. DOI: 10.1073/pnas.1618020114. URL: https://doi.org/10.1073/pnas.1618020114.

[73] Seth Lloyd. "Universal Quantum Simulators". In: *Science* 273.5278 (1996), pp. 1073–1078. DOI: 10.1126/science.273.5278.1073. eprint: https://www.science.org/doi/pdf/10.1126/science.273.5278.1073. URL: https://www.science.org/doi/abs/10.1126/science.273.5278.1073.

[74] Daniel Lobser et al. "JaqalPaw: A Guide to Defining Pulses and Waveforms for Jaqal". In: (2023). arXiv: 2305.02311.

[75] D. Lu et al. "Enhancing quantum control by bootstrapping a quantum processor of 12 qubits". In: *npj Quantum Information* 3.1 (Oct. 2017). DOI: 10.1038/s41534-017-0045-z. URL: https://doi.org/10.1038/s41534-017-0045-z.

[76] Quantum Machines. *Qua: Quantum universal assembly*. URL: https://www.quantum-machines.co/technology/qua-universal-quantum-language/.

[77] Alicia B Magann et al. "From pulses to circuits and back again: A quantum optimal control perspective on variational quantum algorithms". In: *PRX Quantum* 2.1 (2021), p. 010101.

[78] MathWorks. *Quantum Gates*. URL: https://de.mathworks.com/discovery/quantum-gates.html (visited on 04/30/2025).

[79] Sharon Bertsch McGrayne, James Trefil, and George F. Bertsch. *atom. Encyclopedia Britannica*. Accessed 29 April 2025. URL: https://www.britannica.com/science/atom (visited on 04/29/2025).

[80] David C. McKay et al. "Efficient Z gates for quantum computing". In: *Physical Review A* 96.2 (Aug. 2017). ISSN: 2469-9934. DOI: 10.1103/physreva.96.022330. URL: http://dx.doi.org/10.1103/PhysRevA.96.022330.

[81] David C. McKay et al. *Qiskit Backend Specifications for OpenQASM and OpenPulse Experiments*. 2018. arXiv: 1809.03452 [quant-ph]. URL: https://arxiv.org/abs/1809.03452.

[82] Mateusz Meller, Vendel Szeremi, and Oliver Thomson Brown. *Programming tools for Analogue Quantum Computing in the High-Performance Computing Context – A Review*. 2025. arXiv: 2501.16943 [quant-ph]. URL: https://arxiv.org/abs/2501.16943.

[83] Hela Mhiri et al. *Constrained and Vanishing Expressivity of Quantum Fourier Models*. 2024. arXiv: 2403.09417 [quant-ph]. URL: https://arxiv.org/abs/2403.09417.

[84] S. A. Moses et al. "A Race-Track Trapped-Ion Quantum Processor". In: *Physical Review X* 13.4 (Dec. 2023), p. 041052. ISSN: 2160-3308. DOI: 10.1103/PhysRevX.13.041052. arXiv: 2305.03828.

[85] Yair Mulian. *On the exact solution for the Schrödinger equation*. 2024. arXiv: 2402.18499 [quant-ph]. URL: https://arxiv.org/abs/2402.18499.

[86] Michael A. Nielsen and Isaac L. Chuang. *Quantum Computation and Quantum Information*. Cambridge University Press, 2000.

[87] Masanao Ozawa. "Entanglement measures and the Hilbert–Schmidt distance". In: *Physics Letters A* 268.3 (Apr. 2000), pp. 158–160. ISSN: 0375-9601. DOI: 10.1016/s0375-9601(00)00171-7. URL: http://dx.doi.org/10.1016/S0375-9601(00)00171-7.

[88] Maris Ozols. *Postulates of Quantum Mechanics*. Lecture 3, Quantum Computing. Lecture slides. URL: https://www.cl.cam.ac.uk/teaching/1617/QuantComp/slides3.pdf (visited on 04/29/2025).

[89] Line Hjortshøj Pedersen, Niels Martin Møller, and Klaus Mølmer. "Fidelity of quantum operations". In: *Physics Letters A* 367.1–2 (July 2007), pp. 47–51. ISSN: 0375-9601. DOI: 10.1016/j.physleta.2007.02.069. URL: http://dx.doi.org/10.1016/j.physleta.2007.02.069.

[90] Yuxiang Peng et al. "SimuQ: A Framework for Programming Quantum Hamiltonian Simulation with Analog Compilation". In: *Proceedings of the ACM on Programming Languages* 8.POPL (Jan. 2024), pp. 2425–2455. ISSN: 2475-1421. DOI: 10.1145/3632923. URL: http://dx.doi.org/10.1145/3632923.

[91] Adrián Pérez-Salinas et al. "Data re-uploading for a universal quantum classifier". In: *Quantum* 4 (Feb. 2020), p. 226. ISSN: 2521-327X. DOI: 10.22331/q-2020-02-06-226. URL: http://dx.doi.org/10.22331/q-2020-02-06-226.

[92] V N Petruhanov and A N Pechen. "GRAPE optimization for open quantum systems with time-dependent decoherence rates driven by coherent and incoherent controls". In: *Journal of Physics A: Mathematical and Theoretical* 56.30 (July 2023), p. 305303. ISSN: 1751-8121. DOI: 10.1088/1751-8121/ace13f. URL: http://dx.doi.org/10.1088/1751-8121/ace13f.

[93] Vadim N. Petruhanov and Alexander N. Pechen. "Quantum Gate Generation in Two-Level Open Quantum Systems by Coherent and Incoherent Photons Found with Gradient Search". In: *Photonics* (2023). URL: https://api.semanticscholar.org/CorpusID:257074049.

[94] Post-Quantum. *Superconducting Qubits*. Accessed: April 30, 2025. URL: https://postquantum.com/quantum-architecture/superconducting-qubits/.

[95] John Preskill. "Quantum computing in the NISQ era and beyond". In: *Quantum* 2 (2018), p. 79.

[96] Daniel Puzzuoli et al. "Qiskit Dynamics: A Python package for simulating the time dynamics of quantum systems". In: *Journal of Open Source Software* 8.90 (2023), p. 5853. ISSN: 2475-9066. DOI: 10.21105/joss.05853. URL: https://joss.theoj.org/papers/10.21105/joss.05853.

[97] David Puzzuoli. *Qiskit Dynamics: Simulating Open Quantum Systems with Python*. Accessed 2025-05-01. Oct. 2023. URL: https://www.nersc.gov/assets/Uploads/09-Qiskit-Dynamics-Puzzuoli.pdf.

[98] Qblox and Orange QS. *Quantify os and scheduler*. URL: https://quantify-os.org/.

[99] IBM Quantum. *OpenQASM: An Imperative Quantum Assembly Language*. Accessed May 2, 2025. 2017. URL: https://openqasm.com/.

[100] IBM Quantum. *schmidt_decomposition — Qiskit 1.0.3 documentation*. IBM. URL: https://docs.quantum.ibm.com/api/qiskit/quantum_info#schmidt_decomposition (visited on 04/30/2025).

[101] IBM Quantum. *Working with Pulse*. Accessed May 1, 2025. URL: https://docs.quantum.ibm.com/guides/pulse.

[102] QuEra. *Bloqade.jl*. 2023. URL: https://github.com/QuEraComputing/Bloqade.jl/.

[103] QuTiP Developers. *Solver API*. Accessed: May 1, 2025. 2024. URL: https://qutip.readthedocs.io/en/stable/apidoc/solver.html.

[104] Sofia Qvarfort and Igor Pikovski. *Solving quantum dynamics with a Lie algebra decoupling method*. 2022. arXiv: 2210.11894 [quant-ph]. URL: https://arxiv.org/abs/2210.11894.

[105] Michael Ragone et al. "A Lie algebraic theory of barren plateaus for deep parameterized quantum circuits". In: *Nature Communications* 15.1 (Aug. 2024). ISSN: 2041-1723. DOI: 10.1038/s41467-024-49909-3. URL: http://dx.doi.org/10.1038/s41467-024-49909-3.

[106] Saar Rahav, Ido Gilary, and Shmuel Fishman. "Effective Hamiltonians for periodically driven systems". In: *Physical Review A* 68.1 (July 2003). ISSN: 1094-1622. DOI: 10.1103/physreva.68.013820. URL: http://dx.doi.org/10.1103/PhysRevA.68.013820.

[107] Shahid Rahman et al. "A Novel Steganography Technique for Digital Images Using the Least Significant Bit Substitution Method". In: *IEEE Access* (Nov. 2022). DOI: 10.1109/ACCESS.2022.3224745.

[108] Gokul Subramanian Ravi et al. *VAQEM: A Variational Approach to Quantum Error Mitigation*. 2021. arXiv: 2112.05821 [quant-ph]. URL: https://arxiv.org/abs/2112.05821.

[109] Sebastián Restrepo Correales. "Non-unitary evolution control of open quantum systems". In: (2012).

[110] Diego Ristè et al. "Demonstration of quantum advantage in machine learning". In: *npj Quantum Information* 3.1 (Apr. 2017). ISSN: 2056-6387. DOI: 10.1038/s41534-017-0017-3. URL: http://dx.doi.org/10.1038/s41534-017-0017-3.

[111] Rohde & Schwarz. *How to Control a Qubit*. Accessed: April 30, 2025. URL: https://www.rohde-schwarz.com/sg/about/magazine/how-to-control-a-qubit_256450.html.

[112] Wulf Rossmann. *Lie Groups – An Introduction Through Linear Groups*. Oxford Graduate Texts in Mathematics. Oxford Science Publications, 2002. ISBN: 0-19-859683-9.

[113] Rothe. *pulse-fourier: Evaluating Pulse Level Quantum Fourier Models*. 2024. URL: https://github.com/cirKITers/pulse-fourier.

[114] Philip Rübeling et al. "Quantum and coherent signal transmission on a single-frequency channel via the electro-optic serrodyne technique". In: *Science Advances* 10.30 (2024), eadn8907. DOI: 10.1126/sciadv.adn8907. eprint: https://www.science.org/doi/pdf/10.1126/sciadv.adn8907. URL: https://www.science.org/doi/abs/10.1126/sciadv.adn8907.

[115] J. J. Sakurai and Jim J. Napolitano. *Modern Quantum Mechanics*. Indian Subcontinent Version. Pearson, 2014, pp. 67–72. ISBN: 978-93-325-1900-8.

[116] Leonard I. Schiff. *Quantum Mechanics*. 3rd. McGraw-Hill, 1968. ISBN: 978-0-07-055287-6.

[117] Henning Schomerus. *Quantum Mechanics — Lecture notes for PHYS223*. Accessed April 29, 2025. URL: https://www.lancaster.ac.uk/staff/schomeru/lecturenotes/Quantum%20Mechanics/S19.html.

[118] E. Schrödinger. "An Undulatory Theory of the Mechanics of Atoms and Molecules". In: *Physical Review* 28.6 (1926). Archived from the original (PDF) on 17 December 2008, pp. 1049–70. DOI: 10.1103/PhysRev.28.1049.

[119] Maria Schuld, Ryan Sweke, and Johannes Jakob Meyer. "Effect of data encoding on the expressive power of variational quantum-machine-learning models". In: *Physical Review A* 103.3 (Mar. 2021). ISSN: 2469-9934. DOI: 10.1103/physreva.103.032430. URL: http://dx.doi.org/10.1103/PhysRevA.103.032430.

[120] Dominik Seitz et al. "Qadence: a differentiable interface for digital-analog programs". In: (2024). arXiv: 2401.09915 [quant-ph].

[121] Amazon Web Services. *Amazon Braket*. URL: https://aws.amazon.com/braket/.

[122] P.W. Shor. "Algorithms for quantum computation: discrete logarithms and factoring". In: *Proceedings 35th Annual Symposium on Foundations of Computer Science*. 1994, pp. 124–134. DOI: 10.1109/SFCS.1994.365700.

[123] Henrique Silvério et al. “Pulser: An open-source package for the design of pulse sequences in programmable neutral-atom arrays”. In: *Quantum* 6 (2022), p. 629.

[124] Sukin Sim, Peter D. Johnson, and Alán Aspuru-Guzik. “Expressibility and Entangling Capability of Parameterized Quantum Circuits for Hybrid Quantum-Classical Algorithms”. In: *Advanced Quantum Technologies* 2.12 (Oct. 2019). ISSN: 2511-9044. DOI: 10.1002/qute.201900070. URL: http://dx.doi.org/10.1002/qute.201900070.

[125] Dileep Singh. “An In-Depth Analysis of Quantum Computing Frameworks: Exploring Prominent Platforms”. In: 46 (Oct. 2023).

[126] Kaitlin N Smith et al. “Programming physical quantum systems with pulse-level control”. In: *Frontiers in physics* 10 (2022), p. 900099.

[127] Kaitlin N. Smith et al. “Programming physical quantum systems with pulse-level control”. In: *Frontiers in Physics* Volume 10 - 2022 (2022). ISSN: 2296-424X. DOI: 10.3389/fphy.2022.900099. URL: https://www.frontiersin.org/journals/physics/articles/10.3389/fphy.2022.900099.

[128] Thomas Smith et al. *Introducing Qiskit Dynamics: A New Qiskit Module for Simulating Quantum Systems*. Accessed May 4, 2025. 2023. URL: https://medium.com/qiskit/introducing-qiskit-dynamics-a-new-qiskit-module-for-simulating-quantum-systems-afe004f5b92b.

[129] Steinbuch Centre for Computing (SCC), Karlsruhe Institute of Technology (KIT). *bwUniCluster 3.0*. Accessed: May 20, 2025. URL: https://www.scc.kit.edu/bwUniCluster_3.0.php.

[130] John P. T. Stenger et al. “Simulating the dynamics of braiding of Majorana zero modes using an IBM quantum computer”. In: *Phys. Rev. Res.* 3 (3 Aug. 2021), p. 033171. DOI: 10.1103/PhysRevResearch.3.033171. URL: https://link.aps.org/doi/10.1103/PhysRevResearch.3.033171.

[131] PennyLane Team. *Quantum optimal control with differentiable pulse programming (qml.pulse)*. Accessed 2025-05-01. URL: https://docs.pennylane.ai/en/stable/code/qml_pulse.html.

[132] Javier Gil Vidal and Dirk Oliver Theis. *Input Redundancy for Parameterized Quantum Circuits*. 2020. arXiv: 1901.11434 [quant-ph]. URL: https://arxiv.org/abs/1901.11434.

[133] Matteo Votto, Johannes Zeiher, and Benoît Vermersch. “Universal quantum processors in spin systems via robust local pulse sequences”. In: *Quantum* 8 (Oct. 2024), p. 1513. ISSN: 2521-327X. DOI: 10.22331/q-2024-10-29-1513. URL: http://dx.doi.org/10.22331/q-2024-10-29-1513.

[134] Joel J Wallman, Marie Barnhill, and Joseph Emerson. “Characterization of leakage errors via randomized benchmarking”. In: *arXiv preprint arXiv:1412.4126* (2014).

[135] Samson Wang et al. “Noise-induced barren plateaus in variational quantum algorithms”. In: *Nature Communications* 12.1 (Nov. 2021). ISSN: 2041-1723. DOI: 10.1038/s41467-021-27045-6. URL: http://dx.doi.org/10.1038/s41467-021-27045-6.

[136] Eric W. Weisstein. *Statistical Correlation*. [Online; accessed 17-May-2025]. 2023. URL: https://mathworld.wolfram.com/StatisticalCorrelation.html.

[137] M. Werninghaus et al. "Leakage reduction in fast superconducting qubit gates via optimal control". In: *npj Quantum Information* 7.1 (Jan. 2021), p. 14. DOI: 10.1038/s41534-020-00346-2. URL: https://doi.org/10.1038/s41534-020-00346-2.

[138] M. Werninghaus et al. "Leakage reduction in fast superconducting qubit gates via optimal control". In: *npj Quantum Information* 7.1 (2021), p. 14. DOI: 10.1038/s41534-020-00346-2. URL: https://doi.org/10.1038/s41534-020-00346-2.

[139] Marco Wiedmann, Maniraman Periyasamy, and Daniel D. Scherer. *Fourier Analysis of Variational Quantum Circuits for Supervised Learning*. 2024. arXiv: 2411.03450 [cs.LG]. URL: https://arxiv.org/abs/2411.03450.

[140] Annika S. Wiening et al. *Optimizing Qubit Control Pulses for State Preparation*. 2024. arXiv: 2409.08204 [quant-ph]. URL: https://arxiv.org/abs/2409.08204.

[141] Colin P. Williams. *Explorations in Quantum Computing*. Springer, 2011. ISBN: 978-1-84628-887-6.

[142] Windsky. *Quantum Optics: Rotating Frame Transformation*. Accessed: May 4, 2025. Aug. 2023. URL: https://blog.windsky.tech/2023/08/07/Quantum-Optics-Rotating-Frame-Transformation/.

[143] Ying Wu and Xiaoxue Yang. "Strong-Coupling Theory of Periodically Driven Two-Level Systems". In: *Physical Review Letters* 98.1 (2007), p. 013601. ISSN: 0031-9007. DOI: 10.1103/PhysRevLett.98.013601.

[144] Kieran Young, Marcus Scese, and Ali Ebnenasir. "Simulating quantum computations on classical machines: A survey". In: *arXiv preprint arXiv:2311.16505* (2023).

[145] Yuanjing Zhang et al. "Pulse-Level Quantum Robust Control with Diffusion-Based Reinforcement Learning". In: *Advanced Physics Research* n/a.n/a (), p. 2400159. DOI: https://doi.org/10.1002/apxr.202400159. eprint: https://advanced.onlinelibrary.wiley.com/doi/pdf/10.1002/apxr.202400159. URL: https://advanced.onlinelibrary.wiley.com/doi/abs/10.1002/apxr.202400159.

A. Appendix

A.1. Notations

Notation	Description
z^*	Complex conjugate of the complex number z. $(1+i)^* = 1-i$
$\|\psi\rangle$	Vector. Also known as a ket.
$\langle\phi\|$	Vector dual to $\|\psi\rangle$. Also known as a bra.
$\langle\phi\|\psi\rangle$	Inner product between the vectors $\|\phi\rangle$ and $\|\psi\rangle$.
$\|\phi\rangle\langle\psi\|$	Outer product of the vectors $\|\phi\rangle$ and $\langle\psi\|$.
$\|\phi\rangle \otimes \|\psi\rangle$	Tensor product of $\|\phi\rangle$ and $\|\psi\rangle$.
$\|\phi\psi\rangle$	Abbreviated notation for tensor product of $\|\phi\rangle$ and $\|\psi\rangle$.
A^*	Complex conjugate of the A matrix.
A^T	Transpose of the A matrix.
$A^\dagger$	Hermitian conjugate or adjoint of the A matrix, $A^\dagger = (A^T)^*$. $\begin{bmatrix} a & b \\ c & d \end{bmatrix}^\dagger = \begin{bmatrix} a^* & c^* \\ b^* & d^* \end{bmatrix}$
$\langle\phi\|A\|\psi\rangle$	Inner product between $\langle\phi\|$ and $A\|\psi\rangle$. Equivalently, inner product between $\langle\phi\|A^\dagger$ and $\|\psi\rangle$.

Table A.1.: Notation and description summary.

A.2. Pulse-Level Frameworks

Framework	Language	Target Hardware
QiskitPulse (Qiskit Dynamics) [3]	Python	SC, TI
Qutip-qip [55]	Python	SC, TI
SimuQ [90]	Python	NA, DW, SC, TI
Amazon Braket (AHS) [121]	Python	SC, TI, NA
PennyLane [10]	Python	Agnostic
PyQuil-T [27]	Python	SC
Bloqade [102]	Julia/Python	NA
Pulser [123]	Python	NA
qupulse [49]	Python	SC
Artiq [15]	Python	TI
QGL [45]	Python	SC
LabOne Q [52]	Python	SC
Qua [76]	Python-like/custom	SC, NA
OpenPulse [81]	OpenQASM3 [99]	SC, NA
Quantify [98]	Python	SC, NV, Spin
Qibolab [29]	Python/C	SC
PulseLib [30]	Python	Agnostic
JaqalPaw [74]	Python/Jaqal	TI
Cadence [120]	Python	SC

Abbr.: NA - Neutral Atoms, SC - Superconducting, TI - Trapped Ions, NV - Nitrogen-Vacancy Center, DW - D-Wave

Table A.2.: Collection of pulse-level programming frameworks.

A.3. Rotation Visualization

Solving the Schrödinger equation using Qiskit Dynamics' *Solver* class yields the time evolution of the quantum state under the influence of this pulse. From this trajectory, the qubit's population dynamics can be plotted (a), and its state evolution visualized on the Bloch sphere (b) and (c), as seen in Table A.3.

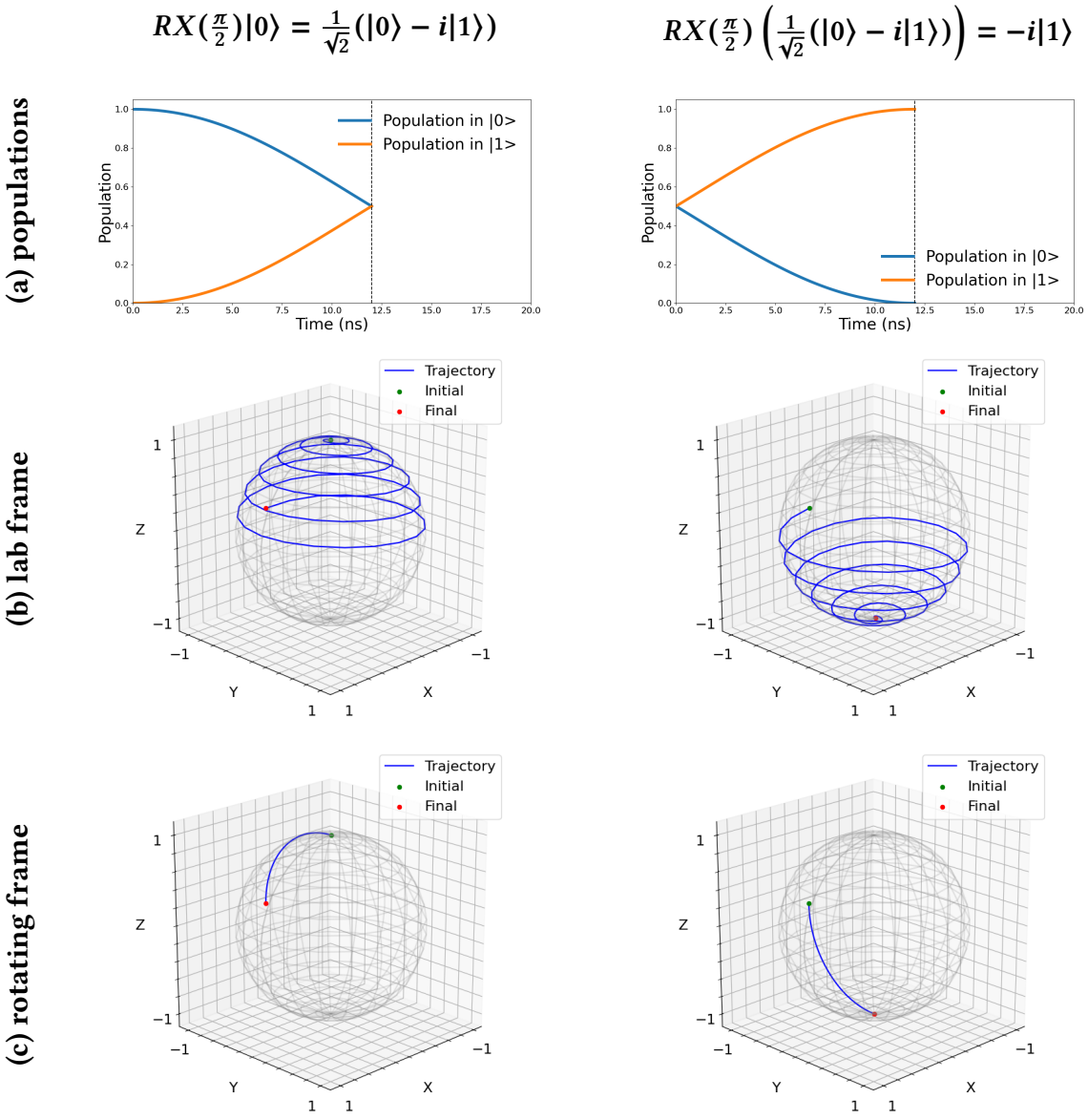

Table A.3.: Visualization of the trajectory of the populations and in the Bloch sphere for both the lab frame and rotating frame, caused by X-Rotations.